



A Voyage from Plasmonic to Hybrid Waveguide Refractive Index Sensors Based on Wavelength Interrogation Technique: a Review

Rammani Adhikari^{1,2} · Zen Sbeah¹ · Diksha Chauhan¹ · Sheng Hsiung Chang³ · Ram Prakash Dwivedi¹

Received: 29 October 2021 / Accepted: 27 January 2022 / Published online: 23 February 2022
© The Author(s) under exclusive licence to Sociedade Brasileira de Física 2022

Abstract

This study describes the underpinning theories and principles in the field of surface plasmon polariton generation and waveguide construction, as well as many design structures based on these waveguides that generate diverse optical resonances and their use for sensing refractive index and temperature variation. Firstly, the investigation of the topologies of plasmonics refractive index sensors based on Bragg grating structures and resonators (cavity and ring) that are coupled to the main bus waveguide is done. Secondly, these architectures' theories and analytical frameworks are summarized. Following that, contemporary sensor development trends based on metal–insulator–metal–resonators (ring or cavity) architecture have been discussed. They have also been compared in terms of performance measures like sensitivity and figure of merit. The results of the comparison demonstrated that sensitivity can be greatly improved, but the figure of merit and quality factor still need to be improved in plasmonic-based sensors. Finally, some recent instances of hybrid plasmonic waveguides connected to a ring resonator have been manifested, which significantly improve the figure of merit and quality factor as compared to plasmonic waveguide–based sensors. Moreover, such structures are easily fabricated due to their CMOS compatibility.

Keywords Figure of merit · Hybrid plasmonic · Quality factor · Refractive index sensor · Plasmonic waveguide · Sensitivity · Surface plasmon polaritons · Temperature-dependent sensors

1 Introduction

The ability shown by nanostructures made up of noble metals to trap and propagate light at the subwavelength range has resulted in a new paradigm shift called plasmonics [1]. This trending technology explains the behavior of surface plasmon (SPs)–combined oscillations of the electrons in the metal–dielectric interface [2]. The SPs as electromagnetic waves traveling at the interface are called surface plasmon waves. The coupling of light with SP waves comprises newer optical waves called the surface plasmon polaritons (SPPs) [3]. These waves show a tendency of traveling across the metal–dielectric interface creating space for various

applications in the area of sensing [4], nanophotonic [5], microcircuitry [6], imaging [7], and much more. SPPs are confined within the interface of metal–dielectric penetrating in the order of nanometer magnitude, and the value depends on the material and on the excitation [8]. The field pattern of SPPs is evanescently decaying in nature. For the efficient generation of SPPs, the prominent layered waveguides (WG) reported are insulator–metal–insulator (IMI) WG, metal–insulator–metal (MIM) WG [9], and dielectric-loaded WG [10]. The IMI WG provides lower loss and larger propagation length. However, they have a mode area of the order of $1\mu\text{m}^2$ [11]. The advanced form of IMI structures is the dielectric-loaded WGs, which have been recently used in interesting applications like thickness measurement and sensing refractive index (RI) of organic thin films in nanoscale [12]. In contrast, the MIM SPP WGs are simpler in their designs and are capable to compress the SPP mode to tenfold of nanometer [13], which paves the way for nanosize applications. So, MIM WG–based devices have drawn much attention from researchers and a diverse range of devices have been proposed based on theoretical studies and experimental demonstrations. These nanosized optical

✉ Ram Prakash Dwivedi
rp.dwivedi@gmail.com

¹ School of Core Engineering, Shoolini University, Bajhol, HP 173229, India

² School of Engineering, Pokhara University, Pokhara Metropolitan City-30, Kaski, Nepal

³ Department of Applied Physics, Chung Yuan Christian University, Taoyuan, Taiwan

schemes include splitters [14, 15], filters [16–20], demultiplexers [21–25], couplers [26, 27], switches [28], modulators [29–31], sensors [32–35], etc. Among these devices, nanosensors with various architectures based on different modulation techniques like WGs width modulation, WG core RI modulation, and hybrid of them have been explored extensively [36].

Recently, plasmonic sensing is one of the most studied areas shown by the Internet survey. The bar graph shown in Fig. 1 narrates the number of papers reported in 2010–2021 which has common searching words as “plasmonic RI sensor” and “plasmonic sensors” from the Scopus database. The data were taken from the Scopus database in Dec 09, 2021. Such a huge investigation to make more understanding of plasmonic sensors and other plasmonic systems has been made possible with the aid of the recent development and advancement of conceptual, algorithmic, and numerical simulating tools like finite element method (FEM)–based COMSOL Multiphysics Commercial software, commercial finite difference time domain (FDTD) solutions, and Lumerical [37].

Here, we focus only on WG core RI modulation techniques in sensing applications based on MIM technology. RI sensors have multiple applications like biosensors for detecting cancer cells [38] and bio-analytes, chemical sensors for detecting different chemicals, and gas sensors for environmental surveillances. The other applications include the calculation of the concentrations and pH values of different solutions based on the variation of RIs. The working mechanism of such sensors relies solely on the variations of the RI of the sensing layer that happen due to the binding of a specific target (chemical species or the family) to this layer and ultimately result in the alteration in the guiding characteristics of the light. When the light is incident on the sensor then due to the overlapping of SPPs inside the sensor at the particular light property (e.g., intensity, wavelength, angle, and phase of light), a narrow peak of confinement loss is achieved, which is called resonance condition. In this particular light property of the entire sensing range, the real value of the effective index of fundamental and plasmon mode is equal. As the RI of the substance to be sensed is changed, there is a shift in the resonance point.

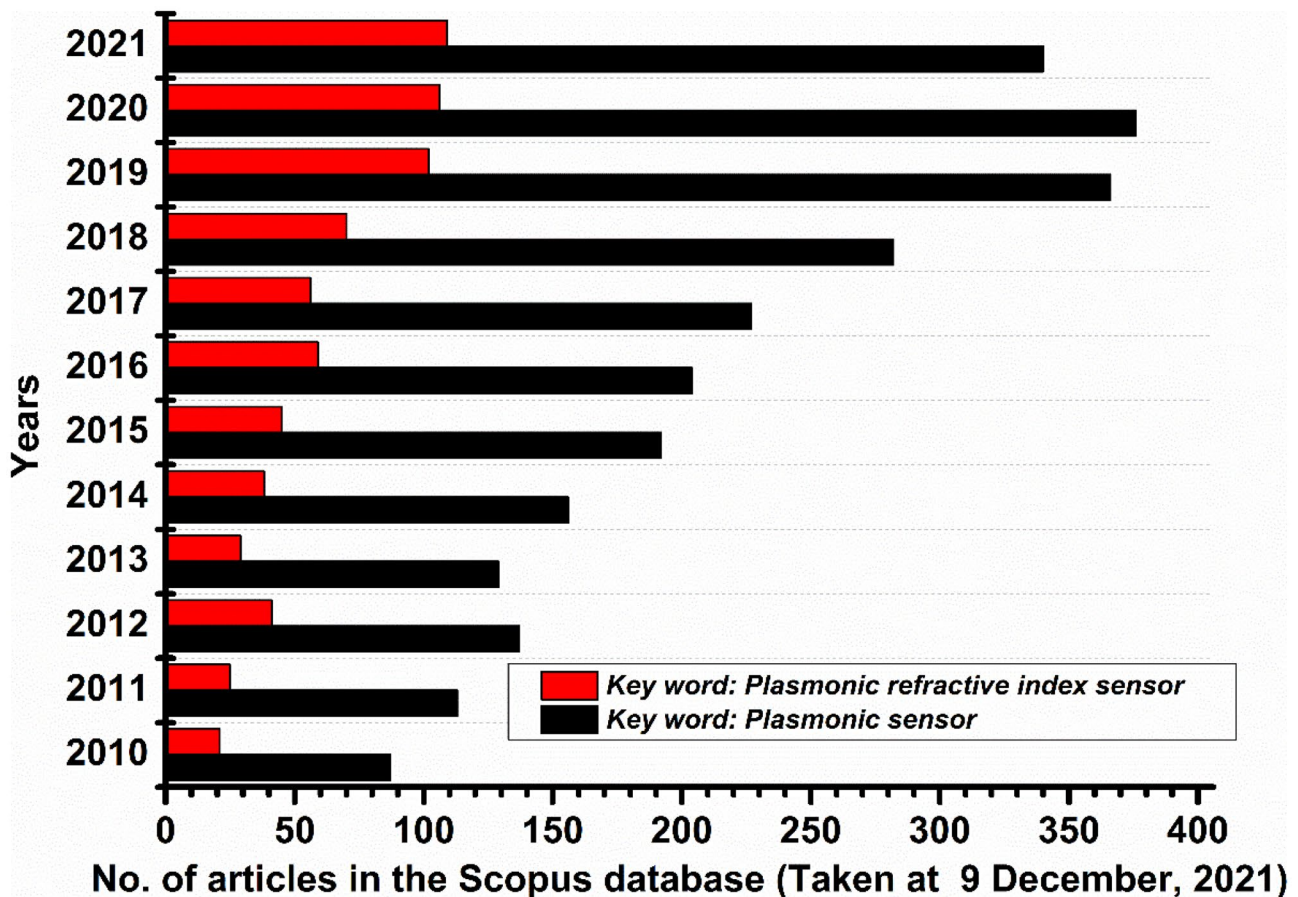


Fig. 1 The pattern of articles published related to plasmonics sensors and refractive index sensors on Dec 09, 2021, obtained from Scopus Database

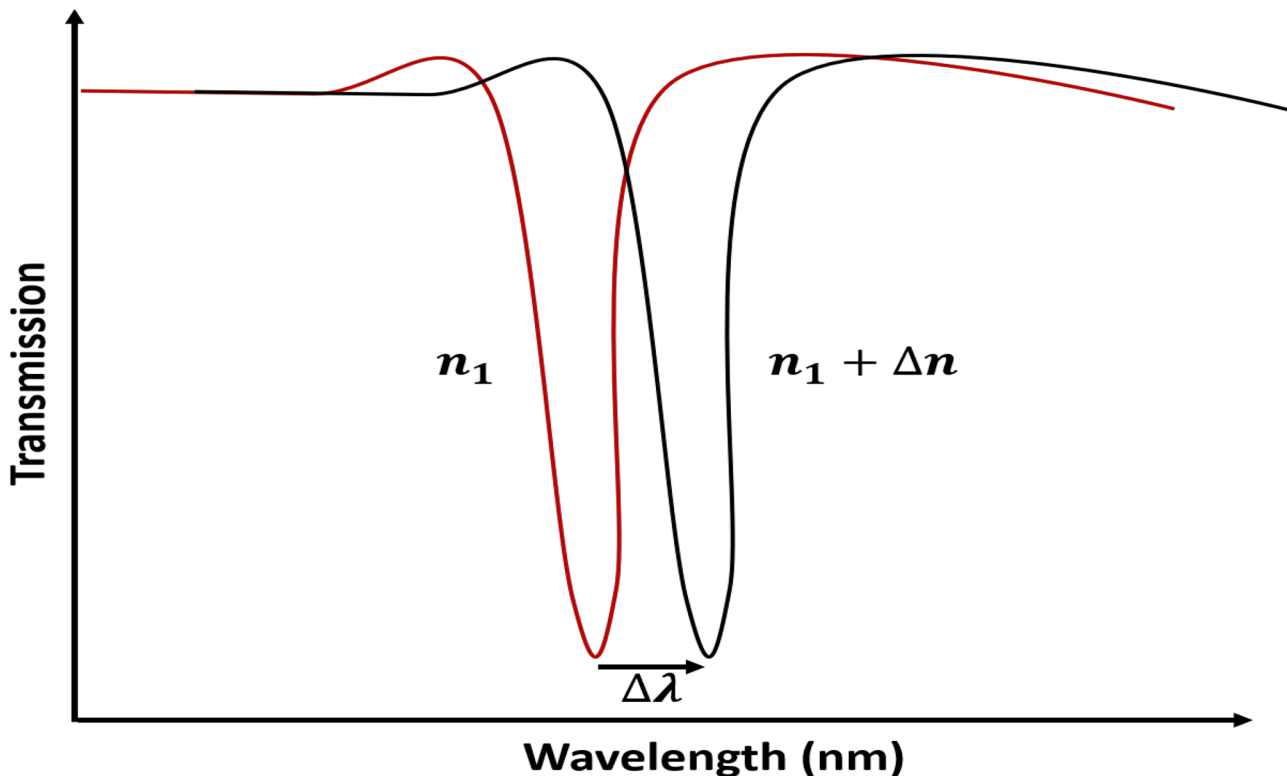


Fig. 2 Illustrating the redshift in resonance wavelength (λ_{res}) owing to change in analyte's RI [39]

If the resonance parameter is the wavelength of light, then the resonance wavelength changes, and its shift occurs [39]. This shift, if it happens towards the right, is called the redshift, and if toward the left, is called blueshift. The redshift phenomenon is described with the help of Fig. 2. It shows that once there is the change of RI from n_1 to $n_1 + \Delta n$, there is a shift in the resonance wavelength quantified as $\Delta\lambda$. Based on observed resonance shifts, an unknown sample can be easily detected.

Before we explain the sensing characteristics, it is worth stating underlying theories about the generation and propagation of the SPPs. In the next section, we also describe the uses of SPPs as sensors.

2 Physics of Surface Plasmons

Here, we discuss the guiding and engineering of light making use of SPPs on the nanometer scale including fundamental physics.

2.1 Surface Plasmon Polaritons

SPPs are electromagnetic confined waves traveling along with a metal–dielectric interface that is generated by the coupling of

free electrons in metals and light waves. For surface charges to emerge, a light wave is required. There are several excitation methods to best feed the light inside the interface for originating SPPs as reported in [40]. The excitation phenomenon ensures the proper feeding of the light wave in the metal–dielectric interface. It needs to satisfy the principle of total internal reflection at the junction of the metal–insulator. Thus, a formed p-polarized wave generates the surface charges (or energized electrons mass) undergoing a combined oscillation. These vibrating charges have correlated radiation fields piercing inside the conductor. They seem exponentially decaying in a direction perpendicular to the interfacing surface as shown in Fig. 3(a and b). These figures illustrate the electric fields and electronic charges at the junction of metal and insulators.

The mechanism of SPP propagation at a metal–dielectric interface is described by the physical quantities like dispersion (k_{SPP}), decay length (δ_{SPP}), field penetration length in metal or skin depth (δ_m), and localization length in insulator (δ_i) [41]. The dispersion relation for SPP can be expressed as follows:

$$k_{\text{SPP}} = k \sqrt{\frac{\epsilon_d \epsilon_m}{\epsilon_d + \epsilon_m}} \quad (1)$$

where $k = \frac{\omega}{c}$ (wave vector in vacuum), ω is the angular frequency and c is the speed of light ($3 \times 10^8 \text{ m/s}$).

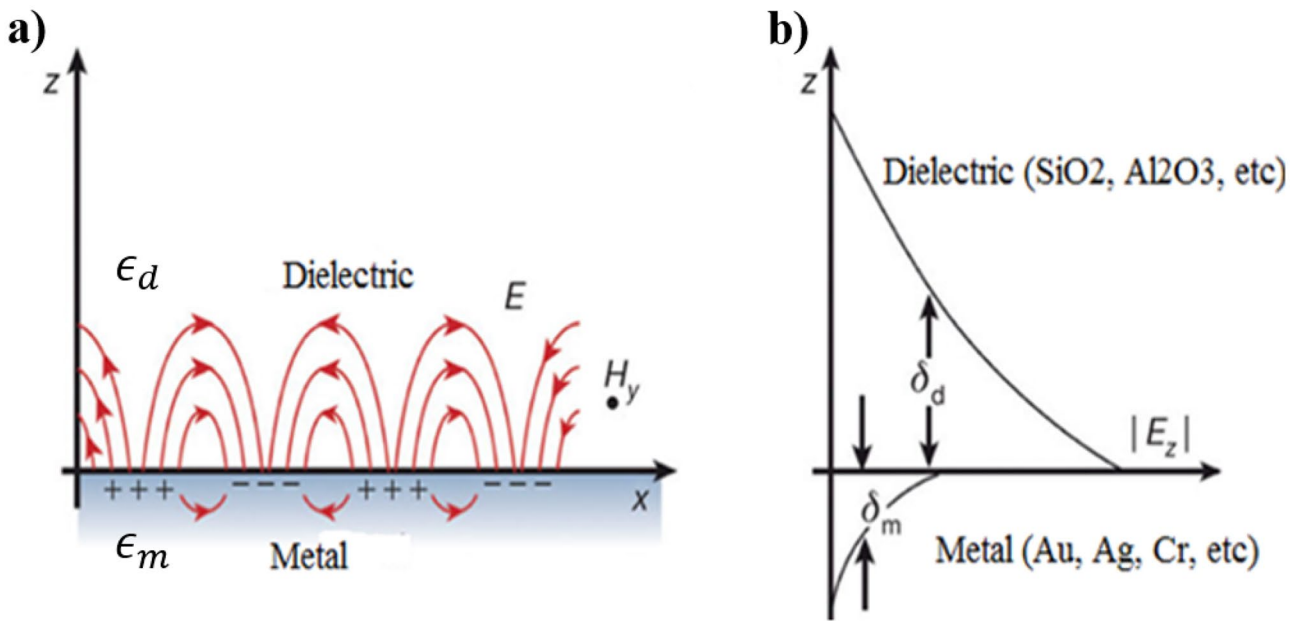


Fig. 3 (a) Exponential decay of electric field in metal and dielectric layers and (b) surface waves and surface charges at the junction of metal–insulator [8]

$\epsilon_m (= 1 - \frac{\omega_p^2}{\omega^2})$ is the frequency-dependent permittivity of metal; ω_p is the frequency of mass plasma.

Similarly, the plasma frequency of SPP is as follows:

$$\omega_{SPP} = \frac{\omega_p}{\sqrt{1 + \epsilon_d}} \tag{2}$$

where ϵ_d is the relative permittivity of the insulator.

The skin depth is a vertical distance up to which the electric field penetrates inside the metal and insulator layer from the top of the surface. The electric field is the highest at the surface and decays exponentially as it goes down the metal/insulator layer. The skin depth (δ_d) of the SPP signal inside the insulator is given by the following:

$$\delta_d = \frac{1}{k} \left(\frac{\epsilon_d + \epsilon_m}{-\epsilon_d^2} \right)^{1/2} \tag{3}$$

and into the metal is given by the following:

$$\delta_m = \frac{1}{k} \left(\frac{\epsilon_d + \epsilon_m}{-\epsilon_m^2} \right)^{1/2} \tag{4}$$

The penetration depth in metal is smaller than in dielectric.

2.2 Propagating Surface Plasmon Polaritons

To propagate the SPPs between the metal–dielectric interface, the first proper coupling is necessary, which then ensures the perfect matching between the electromagnetic field and the

surface’s charges. The different coupling configurations used are prism couplers, grating couplers, fiber, and WG couplers [39]. Among these, the optical WG coupler is recently used to guide the light within a thin metal overlayer of a single or multilayer WG and, thus, the light invades fading through the metal layer [42]. When phase matching between the guided mode and SPP can be done, the fed light will excite the SPP at the external surface of the metal film. Light, thus, converted to SPP mode starts to propagate on a flat metal surface and attenuates gradually reflecting the losses due to the absorption in the metal. Relied on the SPP dispersion relation, the propagation span of SPP is given by $\delta_{SPP} = \frac{\lambda}{2\pi} \left(\frac{\epsilon_{mr} + \epsilon_d}{\epsilon_d \epsilon_{mr}} \right)^{3/2} \frac{\epsilon_{mr}^2}{\epsilon_{mi}}$ [3], where ϵ_{mr} and ϵ_{mi} are the actual and imaginary components of the complex dielectric form of the metal, respectively. All aforementioned equations are valid only in the case of two semi-infinite media, i.e., at a single metal/insulator interface. Moreover, the relation of δ_{SPP} obviously shows that the propagation length is a function of the dielectric constant of the conductor and the wavelength of the incident light. Such propagating SPPs have number of applications. The applications include near field optics, surface-enhanced Raman spectroscopy, computer warehouse, photovoltaic cells, chemical and bio-sensors, and SPP WG [8].

Among these applications, the scope of this study is related to chemical sensors and biosensors (label-free). Chemical sensors are useful in screening chemical compounds in drug sensing based on their RI fluctuations. In general, any biosensor has two functioning blocks: the first is a receptor and target analyte combination, and the second is a physicochemical

transducer. The receptor can mix with its target constituent selectively (e.g., bio-molecules cells and microorganisms). This contact generates bio-information, which the physicochemical transducer then converts into a quantifiable form of the optical, electrical, electromechanical, or thermal signal [43].

Labeled and label-free bio-sensing technologies are the two categories of bio-sensing technologies. Labeled technologies have certain inherent drawbacks, such as being labor-intensive and time-consuming, and sometimes labeling biomolecules can obstruct active binding sites, causing binding characteristics to change. Label-free biosensing methods have been employed to avoid these flaws. To make quantifications easier, they do not require the usage of labels [43]. Instead, they rely on analytes' inherent chemical properties like molecular weight and size, electrical properties like charge and electrical impedance, and optical properties like dielectric permittivity/RI to confirm their presence in a sample. They are also quick, cheap, and easy to use. They contribute to the integration of lab-on-chip principles and allow real-time recognition of target analytes concentrations because of these advantages [44]. This paper investigates label-free biosensors that use the optical RI feature.

2.3 Hybrid Plasmon Polaritons

The usage of SP opens up the possibility of concentrating and manipulating an enormous amount of light. But the optically integrated circuits based on SPs are having an avoidable attenuation due to their absorption losses in the metal. So, the propagation length is relatively reduced. SP waves are pushed closer to the metal's surface by stronger field confinement, resulting in increased absorption and hence shorter propagation length [45]. Thus, if we want to integrate plasmonic components into optoelectronic circuits in practical applications, we must find a compromise between propagation length and field confinement. Among the various strategies adopted to bring such a compromise, hybrid plasmon polaritons (HPPs) that combine the dielectric and plasmonic WG principles have been paid much attention by the researchers [46–48]. For generating HPPs, a typical hybrid plasmonic WG has to be constructed by modifying

either a MIM WG or an IMI WG, which is discussed in Sect. 3.

The sensing application of the SPP and HPP can be quantified and manipulated based on the characteristics of the incident light observed at the output port of WG. So, it is important to know the interrogation techniques that are summarized in the succeeding section.

2.4 Interrogation Techniques

In sensing applications of SPPs, a slight alteration in the RI of the detected medium has a direct impact on the resonance parameters. So, there is a necessity to measure the change in parameters with the change in RI of the material. The RI sensors do measure these parameters. The characteristic parameters are the angle of incidence with which the light enters the WG, wavelength, phase, and intensity of light. Based on the detection scheme, the estimation methods may be grouped as angular, wavelength, intensity, and phase interrogations. Their brief explanation based on modulation technique, light sources used, and calibration curve (measurement curve) is shown in Table 1 as reported in [49].

The methods have their specialties. The angular detection technique requires strong mechanization to read a wide range of resonance angles which brings the extra mechanical burden. The wavelength interrogation technique requires a spectrometer to read the wavelength shifts that increase the overall cost. Moreover, this method is prone to a poor correlation among multicolored rays. The phase interrogation method works with phase shift equipment only in the case of coherently monochromatic light. Since the extraction of phase from the output intensity is erroneous in case of a slight change of input power, the phase interrogation method is complex as compared to the other three methods. The intensity interrogation has also been widely used for sensing the RI of the medium because of its simplicity and low cost [49]. However, the detection limit of the wavelength detection technique is several orders of magnitude smaller than the intensity interrogation techniques, for which it is widely used in RI sensing applications [50]. The scope of this work is limited to examining RI sensors based on the wavelength detection method only.

Table 1 Comparative display of different interrogation methods for plasmonic sensing

Interrogation method	Modulation technique	Type of light source	Calibration curve of sensor
Angular	The angle of incident light is modulated	Coherent	Resonance angle versus RI of the sensing medium
Spectral/wavelength	The wavelength of light is modulated	Polychromatic	Wavelength versus RI of the sensing medium
Intensity	The intensity of the reflected beam is modulated with RI of the sensing substance	Coherent	Intensity versus RI of the sensing medium
Phase	A phase of light waves is modulated with an angle of incidence	Coherent	Phase versus resonance angle

As plasmonic WGs are the foundation for the generation, propagation, and manipulation of SPPs for their applications like sensing and others, the basic and important types of plasmonic WGs are discussed in the following section.

3 Plasmonic Waveguides

SPP WGs are very promising for nanoscale integration for overcoming diffraction limit which was the major drawback in the conventional dielectric WGs. Different WG structures are used for coupling incident light to excite SPPs. As stated before, SPP WGs recently being used are fundamentally layered as MIM or IMI. MIM (where a dielectric layer is sandwiched between the two metal layers)-based plasmonic WGs are extensively used in optical communication and large-scale integrated optical circuits as they can restrict the mode sizes to the few tens of nanometer scale and their propagation lengths are reduced to the micrometer scale, whereas IMI has large mode size in the range of several micrometers [51]. Moreover, these WGs bring a proper equilibrium of light confinement and propagation loss. Alternatively, plasmonic MIM WGs can compress the propagation of light far below the diffraction limit at the cost of relatively extreme ohmic losses [52]. The propagation loss could be further lowered down and propagation distance is substantially increased upon the adoption of the concept of hybrid plasmonic WGs (HPWG). The plasmonic MIM WGs are named as a simple plasmonic WG (SPWG) after the introduction of HPWG. HPWG has increased the substantial interest of researchers because they offer not only subwavelength confinement but also long-span propagation [53]. Structurally, HPWGs have a very thin layer of low-index material called a buffer layer placed between the metal layer and the dielectric layer of the insulator–metal WG. Generally, the air (with $n = 1.0$) can act as a buffer layer. These WGs integrate both dielectric and plasmonic WGs into a single unit thus offering the advantages of both. Interestingly, silicon-based hybrid

plasmonic WGs are deployed most because of their CMOS compatibility required for easy fabrication [54, 55]. The 3-D views of the SPWG and the HPWG in their planar forms are depicted in Fig. 4 (a, b). The operating mechanism of HPWG is explained with the help of mode coupling. The high-index layer WG generates the dielectric mode whereas the metal surface supports SP mode. The buffer layer helps to couple these two modes so that the light will be confined to the low index material between the high-index region and metal layer. The HP mode is tightly confined than the SP mode. The power guided in HPWG in normal form is plotted in Fig. 5, which shows both the SP mode and hybrid mode. If the high-index material is Si, then this technology has similarities with the prevailing Si photonics technology and is fused with Si WG on an identical chip. This incredible guiding scheme has attracted numerous researchers globally who tested packages consisting of compact lasers [56, 57], electro-optic modulation [58], surface-enhanced Raman spectroscopy [59], bio-sensors [60], polarization control appliances [61], photovoltaic cells [62] and thermo-optic switches [63].

For instance, a combination of metal–air/silicon dioxide–silicon layers to form a planar structure of Fig. 4(b) type is one of the popular HPWG based on Si technology. In the structure, Si WG helps to generate the dielectric mode while metallic floor helps to generate SPs. After inserting a buffer layer of air or SiO₂ between these WGs, mode coupling takes place resulting in the fine confinement of light in the buffer layer. Therefore, the HPWG may furnish a superior tradeoff between signal propagation and signal confinement as compared to only the plasmonic mode.

The MIM WGs are found in either planar or channel structure. In the planar geometry of MIM WG, the metal layer is placed on the substrate, the insulator on the metal layer, and on the top again, the metal layer is kept in the stack. This stacking will guide the light in one direction. These kinds of geometry are also called the slab WGs. In contrast to planar WG, channel WG guides light in two dimensions. They have

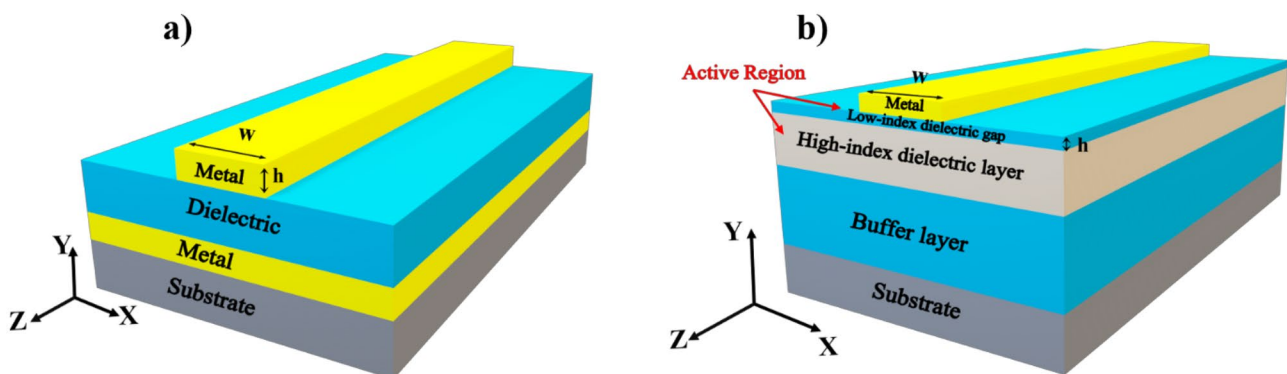
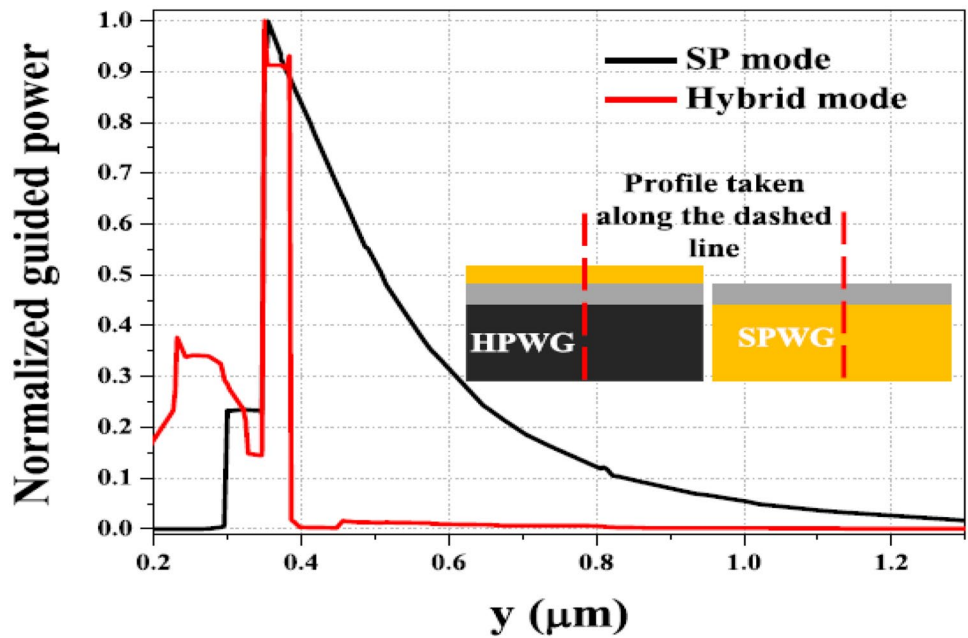


Fig. 4 Waveguides: (a) simple plasmonic waveguide and (b) hybrid plasmonic waveguide

Fig. 5 Pure SP and hybrid mode [64]



a finite width stripe in between the two cladding layers forming a channel to allow the propagation of light, so they are also called stripe WGs. Since both the geometry forms two metal–insulator interfaces, the propagation of SPP shows similar nature. Due to the multi-dimensional propagation of SPP in channel WG, such WG has been widely used for realizing MIM-based structures.

The SP and hybrid mode generation and guiding are dependent upon the material makeup of the WGs. The material properties and their mathematical representation are explained in the next section.

3.1 Material and Methods

The materials to construct the MIM WG are metals, like silver (Ag), gold (Au), copper (Cu), aluminium (Al), etc., and dielectrics, like silicon (Si) [65], air, Al₂O₃, etc. Since the size of the plasmonic WG is lower as compared to the wavelength of the light incident on its input side, only a fundamental mode exists. The basic TM mode in a MIM channel WG as depicted in Fig. 6 is described with the dispersion relation as given in [66] and [67]:

$$\epsilon_{in}k_{z2} + \epsilon_m k_{z1} \coth\left(\frac{ik_{z2}}{2}\right) = 0 \tag{5}$$

having k_{z1} and k_{z2} defined by momentum conservation as

$$k_{z1}^2 = \epsilon_m k_0^2 - \beta^2 \tag{6}$$

$$k_{z2}^2 = \epsilon_{in} k_0^2 - \beta^2 \tag{7}$$

where ϵ_m and ϵ_{in} are the dielectric constants of conductor and insulator, respectively. β indicates propagation constant, and $k_0 = 2\pi / \lambda_0$ indicates the vacuum signal vector of the excitation light. Plasmonic devices are based mainly on Ag, Au, and very few Al for applications working in NIR and visible light.

The planar MIM WG has two interfaces with symmetrical structures as shown in Fig. 7. There are two possible modes: one symmetric and one antisymmetric, which are governed by the corresponding dispersion relations. For fundamental TM mode, these relations are defined by [69] as follows:

$$\tanh\left(\frac{k_d d_d}{2}\right) + \frac{k_m \epsilon_d}{k_d \epsilon_m} = 0 : \textit{Symmetric} \tag{8}$$

$$\tanh\left(\frac{k_d d_d}{2}\right) + \frac{k_d \epsilon_m}{k_m \epsilon_d} = 0 : \textit{Antisymmetric} \tag{9}$$

With $k_{d,m} = \sqrt{\beta^2 - \epsilon_{d,m} k_0^2}$ where β is the propagation constant, k_0 is the free space wavevector, ϵ_d the permittivity of the metal, and ϵ_d is the permittivity of the dielectric.

In MIM WGs, Ag is mostly chosen as a metal layer due to minimum absorption loss. The relative permittivity of Ag has been distinguished based on the Drude model which describes its dependency with the frequency as defined by the following relation.

$$\epsilon_m(\omega) = \epsilon_\infty - \frac{\omega_p^2}{\omega^2 + i\omega\gamma} \tag{10}$$

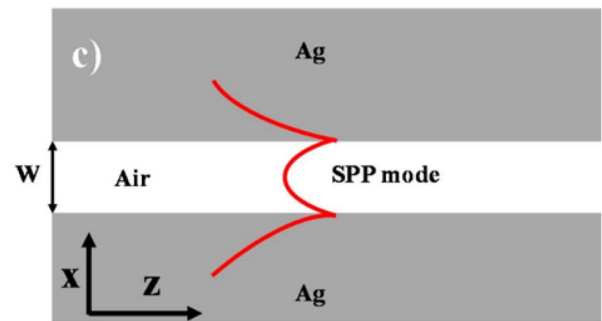
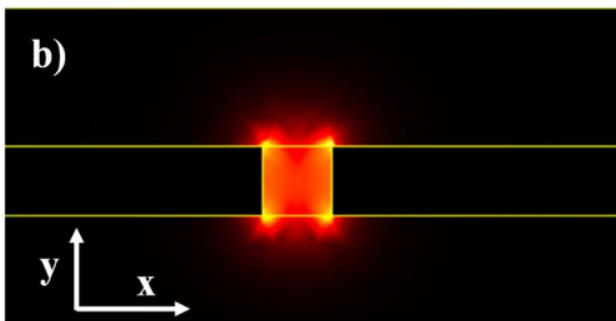
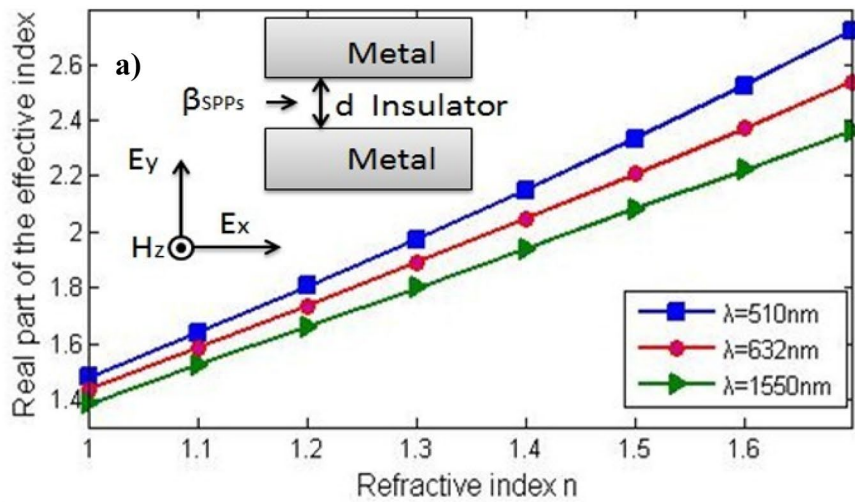


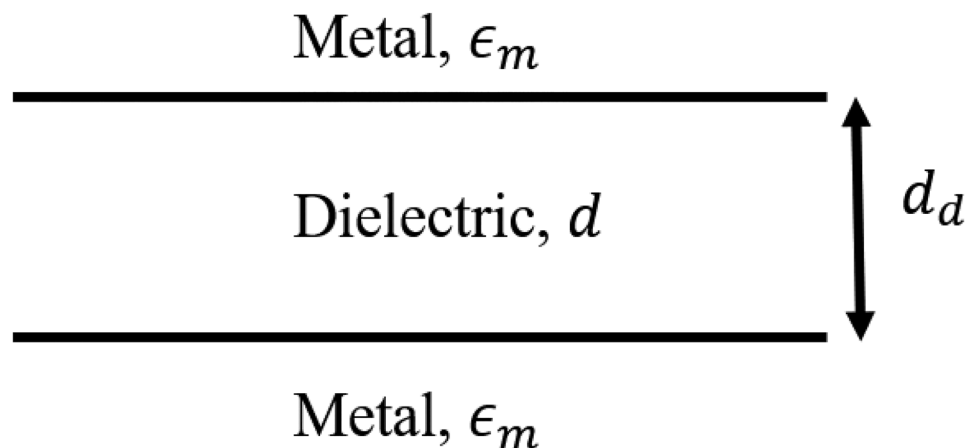
Fig. 6 (a) Plot of the real component of the effective index of SPP vs its refractive indices for varying wavelengths in MIM channel/planar WG [66]. (b) A cross-sectional image of E-field mode across MIM

channel/planar WG [68]. (c) Mode profile for the entire core of MIM channel/planar WG [68]

Here, the constants have their generic names and values such as dielectric constant for infinite frequency, $\epsilon_\infty (= 3.7)$; plasma frequency due to moving electrons, $\epsilon_p (= 9.1\text{eV})$; electron collision frequency, $\gamma (= 0.018\text{eV})$; and free space angular frequency of an incident optical wave, ω [66]. The effective RI relies on propagation constant (i.e., a real part

of β) which can be expressed as $n_{\text{eff}} = \text{real}(\beta/k_0)$. Figure 6(a) shows the dependence of the practical RIs of SPPs on RI (n), demonstrating that these two parameters have a linear relationship at the incident wavelengths. In Fig. 6(b and c), the electric-field spreading of SPPs along with their

Fig. 7 Schematic diagram of asymmetric MIM planar WG



profile towards the propagation direction is depicted. According to Lorentz–Drude model, the permittivity function of Ag is given as follows [70]:

$$\varepsilon(\omega) = \frac{\omega_p^2}{\omega(\omega - i\Gamma_0)} + \sum_{n=1}^6 \frac{f_n \omega_n^2}{\omega_n^2 - \omega^2 + i\Gamma_n} \quad (11)$$

where ω_p and ω_n are the plasma and resonance frequency and Γ_0 , Γ_n , and f_n are respectively the damping constant, damping frequency, and oscillators strength. According to Debye–Drude model, the complex relative permittivity of Ag is as follows [71]:

$$\varepsilon(\omega) = \varepsilon_\infty + \frac{\varepsilon_s - \varepsilon_\infty}{1 + i\omega\Gamma} + \frac{\sigma}{i\omega\varepsilon_0} \quad (12)$$

where ε_∞ , ε_s , σ , and Γ are the infinite frequency permittivity, the static permittivity, the conductivity, and the relaxation time, respectively. Their numerical values are as follows: $\varepsilon_\infty = 3.8344$, $\varepsilon_s = -9530.5$, $\sigma = 1.1486 \times 10^7$ S/m, and $\Gamma = 7.35 \times 10^{-15}$ s [71].

Having discussed the basics of MIM SPP generating features, it is important to have an idea about the evaluating parameters for sensing applications. The performance parameters are explained in the next section.

4 Performance Metrics of Sensor

The plasmonic MIM WG–based sensors mostly used Ag as a metal, and its modeling is as defined in Eq. (10), Eq. (11), and Eq. (12). Different structural models based on MIM WG for sensing applications have been proposed by the researchers which are based on the resonance phenomenon which is popularly known by ring resonator [72], stub-resonator [73, 74], Fabry–Perot resonator [75], and Fano-resonators [76–78]. The other class of sensors is interferometric sensors [79–81]. Optical interferometric sensors are extensively useful for sensing various physical characteristics such as temperature, strain, pressure, and RI. They can be of four different types, viz., Fabry–Perot, Mach–Zehnder, Michelson, and Sagnac. Their detailing has been done in [82]. Herein, the RI and temperature sensors based on MIM WG resonator system have been discussed. Before starting the design models and the concepts behind these systems, the performance metrics of the sensors are discussed. Sensitivity and figure of merit (FoM) are the main performance measuring quantities of MIM plasmonic–based RI sensors. To be more explicit, the efficiency of RI plasmonic sensors is measured in terms of these two parameters; however, the calculation methods can be theoretical, experimental, or a combination of both.

4.1 Sensitivity

The sensitivity (S) of a sensor is the ratio of the change in the sensor output to the change in the amount to be measured (e.g., the concentration of the analyte). This is called bulk sensitivity [83]. The sensitivity of an SPP-based sensor relies on two factors—sensitivity of the sensor output (e.g., resonant angle or wavelength or intensity) to the RI and efficiency of conversion of the sample binding to a change in RI. The thin film sensitivity of an SPP-based sensor to a RI (S_{RI}) can be expressed as a product of two terms [83]:

$$S_{RI} = \frac{\delta Y}{\delta n_{\text{eff}}} \frac{\delta n_{\text{eff}}}{\delta n_d} \quad (13)$$

where Y denotes the sensor output quantity, and n_d denotes the RI of dielectric. The first term describes the sensitivity of the sensor output to RI of the SPPs and depends on the excitation of SPPs and used modulation method, whereas the second term describes the sensitivity of the effective RI (n_{eff}) of SPPs to the RI and it is independent of both the figures. In our case, the output quantity of the sensor is resonant wavelength and the measuring quantities are RI and temperature for RI sensors and temperature-dependent sensors, respectively. So, bulk sensitivity is described as the rate of change of resonant wavelength per unit rate of change of measuring parameter such as a RI for RI sensors and temperature for temperature sensors. Symbolically, $S_{RI} = \delta\lambda_{\text{res}}/\delta n_{\text{eff}}$ (nm/RIU) for RI sensors [84], where $\Delta\lambda_{\text{res}}$ is the resonance wavelength wherein the maximum excitation of SPPs occurs. Similarly, temperature dependent sensitivity is described as $S_{\text{temp.}} = \delta\lambda_{\text{res}}/\delta K$ (nm/°C) [66], wherein $S_{\text{temp.}}$ specifies shifting of resonant peak ($\delta\lambda_{\text{res}}$) produced by the unit change of the surrounding temperature (δK). The sensitivity values for different geometries are quantified as depicted in Tables 2, 3, 4, and 5.

4.2 Figure of Merit

In sensing applications, FoM is used to judge the sensing execution and it is defined as $\text{FoM} = S/\text{FWHM}$ (1/RIU) for Lorentzian line–like response [85], where FWHM is the full width at half maximum of the spectrum and S is the sensitivity. FWHM is associated with the propagation span, i.e., a lifetime of SP that normally defines the sharpness of the dip/peak. In some real applications, the change of light power at a particular wavelength is recorded to calculate the respective FoM [84], and it is expressed as $\text{FoM} = (\Delta T/\Delta n)/T$ for Fano line–like response [86], wherein T is the transmittance at the spectral wavelength and $\Delta T/\Delta n$ is variation in transmittance caused by change

Table 2 Comparison of the characteristics of MIM channel WG-based plasmonic RI sensor reported in the literature

Ref	Resonator type	Materials	Analysis method	Metal model	Types of resonance	S (nm/RIU)	FoM (/RIU)	Operating Wavelength (nm)
[66]	Single ring resonator	Ag/air	FEM	Drude	Lorentzian	3460	...	500–2000
[68]	Square ring cavity	Ag/air	FEM	Lorentz–Drude	Lorentzian	1367	25	1300–2000
[70]	Square ring cavity with Ag nanorods	Ag/air	FDTD	Lorentz–Drude	Lorentzian	2320	...	1000–3000
[71]	The square ring filled with nanodots	Ag/air	FEM	Debye–Drude	Lorentzian	1240	20	900–1400
[72]	Square ring resonator	Ag/air	FEM	Lorentz–Drude	Lorentzian	1200	19.7	1200–1800
[84]	Rectangular cavity and disk cavity	Ag/air	FEM	Drude	Lorentzian	1136	51.27	800–1500
[85]	Concentric double ring resonator	Ag/water	FDTD	Drude	Lorentzian	1060	203.8	700–1200
[65]	Ring resonator containing circular tapered defects	Ag/Si/air	FDTD	Drude	Lorentzian	1295	159.6	1200–2400
[87]	Double cavity with rectangular defect	Ag/air	FDTD	Drude–Lorentian	Lorentzian	2602.5	...	1200–2800
[89]	An array of nanoholes in hexagonal cavity resonator	Ag/air	FDTD	Drude	Lorentzian	3172	...	900–2000
[90]	Hexagonal ring cavity	Ag/air	FDTD	Lorentz–Drude	Lorentzian	4270	37	800–2000
[91]	Square rings	Ag/air	FEM	Lorentz–Drude	Lorentzian	1320	16.5	1200–1800
[93]	Triangular resonator	Ag/air	FEM	Lorentz–Drude	Lorentzian	2713	35.1	800–2500
[98]	Composite of asymmetric H-type and circular ring resonators	Ag/air	FEM	Drude and CMT	Lorentzian	1379	...	800–2200
[100]	T cavity filled with nanorods	Ag/air	FEM	Debye–Drude	Lorentzian	8283	...	1000–8000
[101]	Two ring resonators	Ag/air	FEM and Coupled Mode Theory (CMT)	Drude	Lorentzian	685	...	500–1750
[102]	Elliptical ring resonator	Ag/air	FDTD	Drude	Lorentzian	1100	224	800–1250
[103]	Racetrack resonator	Ag/air	FDTD	Drude	Lorentzian	4650	37	1400–3200
[104]	Half ring resonator and rectangular cavity	Ag/air	FDTD	Drude	Lorentzian	753	...	500–1000
[105]	Side-coupled bow tie cavity resonator	Ag/air	FEM	Lorentz–Drude	Lorentzian	2300	31.5	1600–2050
[106]	Side-coupled semi-ring resonator with nanodots cavity	Au/air	FEM	Drude	Lorentzian	1084.21	161.17	600–1200
[107]	Side-coupled two asymmetric shunt cavity resonators	Ag/air	FDTD	Drude	Fano	780	4800	760–880
[108]	Edge-coupled fillet cavity	Si/Ag/material	FEM	Drude		1496	124.6	750–2500
[76]	Side-linked square convex circular ring resonator with a metallic baffle	Ag/air	FEM & CMT	...	Fano	1120	2.68×10^5	900–1200
[109]	Side-coupled circular ring resonator	Ag/air	FDTD	Debye–Drude	Lorentzian	600–900

Table 3 Performance comparison of different plasmonic sensors based on metallic nanostructures and MIM-WG structures

Ref	Modalities	Type of resonance	Sensitivity (nm/RIU)	FoM (1/RIU)	Applications
[111]	MIM Bragg grating structure side linked to plasmonic nanocavity	Fano	1425	1170	Integrated nanoscale sensors
[112]	S-shaped MIM plasmonics grating	Lorentzian	1960	27.7	Chemical and temperature sensors
[113]	MIM plasmonic Bragg grating with silver as a metal	Lorentzian	1488	20	Chemical and biological sensors
[88]	Nanostructured plasmonic chip with Au layer	Lorentzian	425	35	Biosensors
[114]	Au/Ag bi-grating layer	Lorentzian	356	.	Biosensors
[115]	Transmit—array meta-surface	Lorentzian	192	64	Biosensors
[116]	Semicircular grooves and apertures	Lorentzian	428.70	24	Biochemical sensors
[117]	Au ring—MgF ₂ -Au plate	Lorentzian	190	14.61	RI sensors
[118]	Al ₂ O ₃ grating	Lorentzian	461.53	182.50	Biosensor

in RI in the given wavelength. To boost the FoM, the sharpness of the peak/dip should be high which is made possible by coupling different structures made by different materials to the main MIM WG. Now, the different structures are surveyed and compared based on these two performance characteristics of them as RI sensors and temperature-dependent sensors. The FoM values for various proposed geometries are displayed in Tables 2, 3, and 5. Having stated the performance parameters of the sensors, the next section explains the different structural makeups that play roles in generating resonances.

4.3 Structural Models and Their Theories

As depicted in Fig. 8, the structural models of the plasmonic sensors are designed such that they exploit SPP/HPP principle. These waves are generated, manipulated, and regulated with the aid of WG-based plasmonic resonating structures. Such resonating structures, thus, realized are used as RI and temperature sensing applications as they offer resonance responses of Lorentzian line shape or Fano line shape that gives a condition of maximum SPP energy confinement in the resonator. The different forms of resonators and their sensing mechanisms are explained in the proceeding section.

4.3.1 Ring and Cavity Resonator–Based RI Sensors

Most widely and abundantly explored and reported MIM plasmonic–based sensor structures are ring resonator structures. Multiple resonators have been presented and analyzed such as rectangular resonator [84], ring resonator [65, 77], disk resonator [87, 88], hexagonal ring resonator [89, 90], square ring cavity [91, 92], triangle-shaped resonator [77, 93], and tangent ring resonator [94]. Other structures are constructed by combining two or more aforementioned structures. The working of these structures is explained as follows: as the light signal travels across the main WG, only a small portion of it gets stuck into the ring/cavity when they are kept sufficiently close to each other. This is called the coupling of the wave between the WG and the resonator. When the light travels through a WG and enters the ring/cavity without changing its phase (i.e., the light traveling in-ring should have the same phase as it has when the light was entered in the ring/cavity), at some wavelength(s), the resonance(s) is produced. When the RI of the material inside the ring/cavity is changed, then it will induce a shift in the resonance wavelength. This shifting phenomenon of resonance wavelength with respect to change in RI is utilized for sensing. The medium material is probably the most crucial element to investigate because

Table 4 Performance comparison of MIM plasmonic temperature–dependent sensors

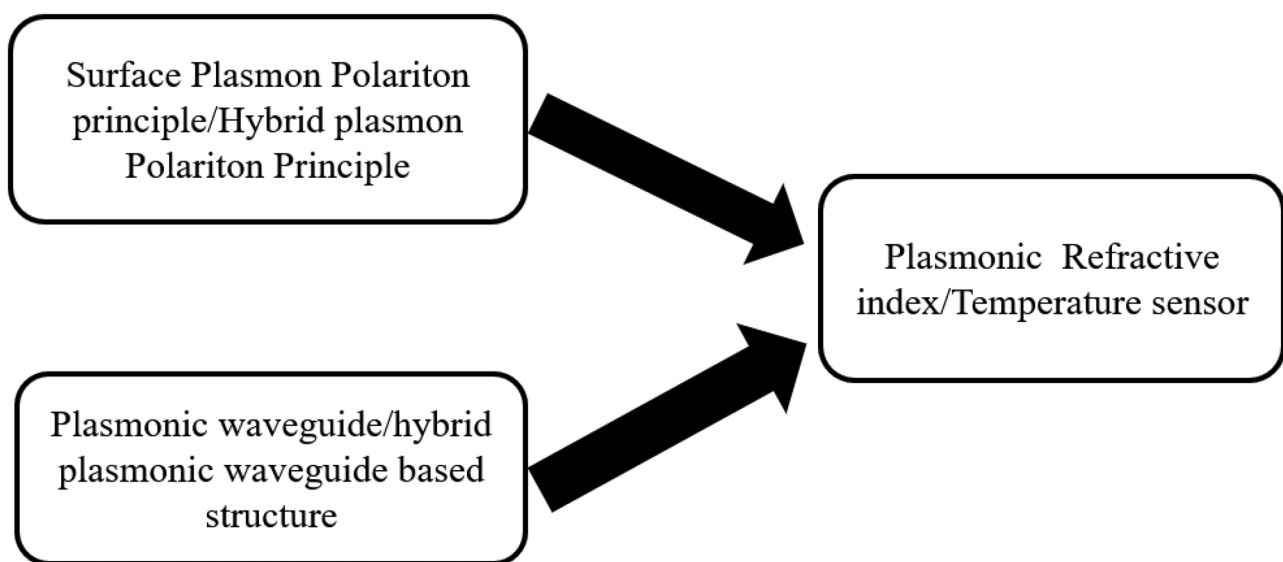
Ref	Topology	Liquid used	Temperature sensitivity (nm/°C)
[70]	Square ring with nanorods array	Ethanol	0.84
[100]	T-shaped cavity with metal nanorods defects	Ethanol	3.30
[90]	Hexagonal ring cavity	Ethanol	0.56
[98]	Circular ring + H-type resonator	Ethanol	−0.55
[103]	Racetrack resonator	Deionized water	0.69
[66]	Ring resonator	Ethanol	1.36
[119]	Ring resonator	Ethanol	−0.53

Table 5 Comparison of the characteristics of HPWG-based RI sensors

Ref	Topology	HPWG structure	Analysis method	Types of resonance	S (nm/RIU)	FoM (/RIU)	Q -factor
[122]	Metal assisted stripe WG side coupled to the ring resonator	Si-SiO ₂ -Au	FEM	Lorentzian	300	36.6	217.3
[64]	Race track HPWG-based microring resonator	Si-SiO ₂ -Au	FEM	Lorentzian	230	53.48	306.5
[123]	Double – slot HPRR (side coupled)	Si-SiO ₂ -Ag	FDTD	Lorentzian	687.5	...	1034
[121]	WG ring resonator with slot and stripe WGs	Si-SiO ₂ -Si	FEM	Fano	106.29	1337	18,500
[124]	Two-slot WG-based microring	Si-air-gold ring (outer slot WG) and gold ring-air-gold disk (inner WG)	FEM	Lorentzian	800	37	70
[125]	Subwavelength Grating HPWG-based ring resonator	Si-SiO ₂ -Au	FEM	Fano	1000	287.35	441.05
[126]	Racetrack ring resonator based on WG double slot subwavelength grating	Si-SiO ₂ -Au	FEM		1000	...	5445
[127]	Hybrid plasmonic microring resonator	Au-air-Si	FEM	Lorentzian	690	98.6	222

it has a significant impact on lightwave transmission. Furthermore, the coupling length has an impact on the coupling. In addition to this, the proper coupling between the WG and ring/cavity offers different effects in the evanescent waves (or SPP) of MIM WGs like the plasmonic-induced transparency (PIT) effect and Fano effects. These effects are caused by three separate mechanisms: destructive interference between bright and dark modes [95], destructive interference between various modes in a multimode resonator [96], and well-defined phase coupling between resonators

[97]. According to Tian and Li [98], the structure consists of a MIM WG, a parallelly standing asymmetric H-type resonator (AHR), and a circular ring resonator (CRR), with the former shape, promptly linked to the main WG and the later shape linked to the AHR, resulting in the PIT by the harmful interference of two transmission pathways. Luo et al. [84] show a similar effect by reporting a structure consisting of a MIM WG coupled with a side-linked rectangular cavity and a disc cavity, where the transmission peak for disc divides into two, and this may be a kind of

**Fig. 8** Conceptual diagram of plasmonic RI/temperature sensor

standard PITs. Similarly, Bin Feng et al. [99] employ the PIT effect in a sensing application with a structure that consists of a MIM and two ring resonators, allowing the SPP wave to be linked, first, into the bottom ring and, second, to the top ring via near field interplay. The waves are then trapped within the ring resonator, causing resonance to occur owing to the resonance condition specified by Eq. (14). The bottom ring resonator will be bright, while the top will be dark. A noticeable transmission sink appears on spectral curves as a result of the PIT effect. However, these effects do not fall under this study. This study only looks at the Lorentzian resonance effect. For this effect to happen, WG mode and resonator mode have to be coupled precisely giving a resonant condition. Different resonators have different resonating conditions because they are influenced by several structural parameters. Based on the survey, the mathematical resonating conditions for different resonators are listed as follows:

For the ring resonator, the resonant condition is illustrated by the following relation [66]:

$$\frac{J'_n(kr_a)}{J'_n(kr_i)} - \frac{N'_n(kr_a)}{N'_n(kr_i)} = 0 \tag{14}$$

As shown in Fig. 9, r_a and r_i are the external and internal radii of the ring resonator. where the symbol $k = \omega\sqrt{(\epsilon_0\epsilon_r\mu_0)}$, for permeability of μ_0 (air), and relative permeability $\epsilon_r = n_{\text{eff}}^2/\mu_0$ that mainly relies on frequency, and J_n and N_n are the Bessel function of the first kind and second kind with an order n , respectively. For a rectangular cavity, the resonant condition can be given by the following [84]:

$$\frac{2\pi}{\lambda_m} \cdot 2h \cdot \text{Re}(n_{\text{eff}}) + \varphi_r = m \cdot 2\pi \tag{15}$$

where λ_m = resonant wavelength; φ_r = phase shift due to the reflection on the two sides of the rectangular cavity; and

m = a positive integer which represents the order of the resonance. For the disk cavity, the resonant condition can be given by the following [84]:

$$k_d \frac{H_n^{(1)'}(k_m r)}{H_n^{(1)}(k_m r)} = k_m \frac{J_n'(k_d r)}{J_n(k_d r)} \tag{16}$$

where k_d and k_m are the wave vectors in the disk cavity and metal, respectively, $H_n^{(1)}$ and $H_n^{(1)'}$ are the first kind Hankle function with order n and its derivative, J_n and J_n' are the first kind Bessel function with order n at its derivative, respectively. For ring resonator of square shape, the resonant wavelength can be calculated by the relation given by the following [72]:

$$\lambda_{\text{res}} = \frac{4L_{\text{eff}}\text{Re}(n_{\text{eff}})}{N} N = 1, 2, 3 \dots \tag{17}$$

The notations n_{eff} and L_{eff} signify the ultimate RI in the square ring resonator, and L_{eff} indicates the functional side length, which is calculated by averaging the interior and exterior lengths of the rectangle as shown in Fig. 10.

For the square cavity, the resonance wavelength can be given by the following [70]:

$$\lambda_{\text{res}} = 2\text{Re}(n_{\text{eff}})L/(m - \varphi/\pi) \tag{18}$$

where φ is the phase shift per round trip, n_{eff} is the practical RI of SPPs, λ_{res} is the resonance wavelength, and m is an integer.

For T-shaped cavity, the resonance wavelength is calculated as as follows [100]:

$$\lambda_{\text{res}} = \frac{2Ln_{\text{eff}}}{n - \varphi_{\text{ref}}/\pi} \tag{19}$$

where L is the effective length of the cavity, n_{eff} is the real part of effective RI of SPPs, and φ_{ref} is the phase shift of SPP reflection at the cavity metal wall. And n is the mode number ($n = 1, 2, \dots$).

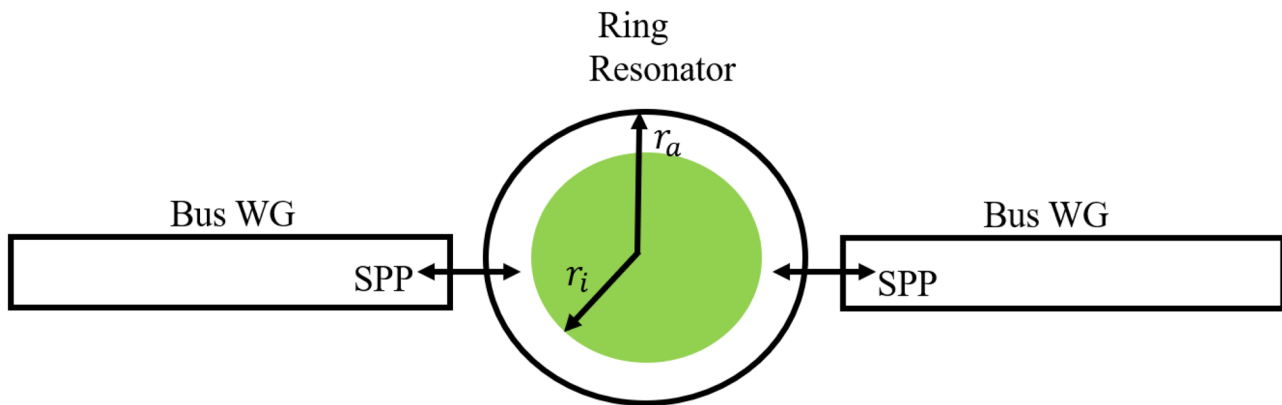


Fig. 9 A schematic of a ring resonator directly coupled with the two main WGs

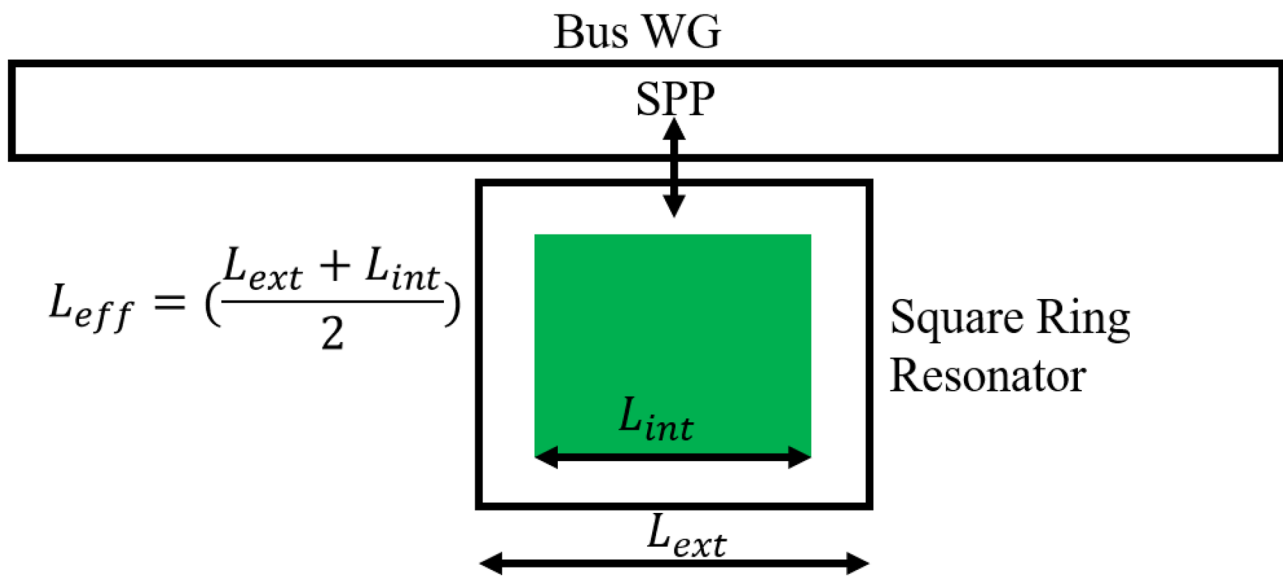


Fig. 10 A schematic of a square ring resonator side coupled with a MIM WG

For triangular cavity, the resonance wavelength can be calculated as follows [93]:

$$\lambda_{\text{res}} = \frac{\text{Re}(n_{\text{eff}} \cdot p_{\text{eff}})}{m - (\frac{\varphi}{2\pi})} \quad (20)$$

where n_{eff} is the effective RI, p_{eff} is the effective path traveled by the SPPs in the resonator, φ is the total phase shift in the edges of the resonator, and m is a positive number.

The MIM WG is either directly coupled or side coupled with ring/cavity structures [86] which are used to measure the change in RI. The WG mode and the resonant mode gets coupled to each other. If the phase-matching condition is fulfilled, then a certain wavelength of the SPP wave resonance occurs. The resonant wavelength is related to the RI of the medium filled in the resonator. If the material medium is changed, then there will be a subsequent shift in the resonant wavelength which we can observe and measure at the output port of the WG. The parameters of the resonator also affect the resonant wavelength which can be seen from the Eqs. (14–20). Based on the material medium inside the resonator and the resonator's parameters, they pose different sensing abilities which we have summarized in Table 2. Table 2 also compares the sensor in terms of their other characteristics like geometry, material makeup, operating wavelength, etc.

The structure can be classified into five classes based on the designs shown in Table 2: ring resonators coupled to MIM WG, cavity resonators coupled to MIM WG, ring resonators with some defects such as nanorods, cavity resonators with some embedded structures such as nanowalls, and nanorods, and ring cavity system coupled to MIM WG. The sensitivity

of typical ring and cavity resonators ranges from a few hundred to a few thousand. However, the FoM is in the range of a few tens to a few hundred. With slight changes or additions to the device structure, the sensitivity has been improved because they help in enhancing light–matter interaction. The introduction of metallic elements has improved the intensification of SPPs. Metallic elements in different shapes like nanorods in a circular shape and nanowalls in rectangular shape have been used to decrease the sensor size and increase the RI sensitivity. Since metal like Ag has the smallest damping constant and is the best choice in the optical frequencies, it is abundantly used in the MIM-resonator-based plasmonic sensors. The Ag nanorods can act as surface plasmon resonators and electromagnetic energy transporter when they are embedded in the dielectric substrate [100]. The size of the nanorods directly affects the E-field enhancement of SPPs around them. The larger the radius of the nanorods, the larger will be the field enhancement and vice versa. Such an enhancement may provide the possibility to increase RI sensitivity. If nanorods are arranged in an array form as metallic grating, they further assist in the intensification of SPPs. Sometimes, the nanorods may be made up of Si [65]. Adding such nanorods to the WG increases the transmission spectrum and the ring will change the resonance location. Moreover, if they are ordered in a planar form, then they are easily implemented in high-density on-chip circuits and ultra-compact structures. The nanowall provides high confinement of electric field distribution of SPP mode in the narrow region of the cavity. When different dielectric materials are made in the form of nanoholes, the effective RI will change and leads to change in plasmon properties. Such nanoholes when gets the shape of resonator after their arrangement, they are compact

in size and show a high sensitivity level to surface features because of high confinement of local electromagnetic fields and interact with the ambient environment. With the proper array of nanoholes, adjustable resonance wavelength and small detection volume can be used [89]. Since the abovementioned structures produce the symmetrical Lorentzian-shaped transmission profile which is not sharp enough, the values of FoM are lower. The problems observed were that the aforementioned strategies could not increase both performance attributes at the same time. The analysis was carried out using the FEM or the FDTD method. Ag serves as the substrate, and it is mostly modeled by a Drude or a Deby–Drude model. The wavelength interrogation approach was used as the detection scheme. If the design is such that it would generate the sharp Fano peaks as reported in [76], the FoM is observed to improve with the acceptable value of S .

As seen from the MIM structures that excite the SPP waves, the optical properties of such waves are strongly governed by the metal type used, the width, and the material of the inserted dielectric. However, the width of regular MIM WG is kept fixed once selected. To get rid of such a limitation of uniform MIM WG, we can introduce some periodic structures in the dielectric layer of the WG. Such structures can be either realized by altering the width of the dielectric layer periodically [99] or by infiltrating two different dielectric materials periodically along with the MIM WG [110] to build a MIM type Bragg grating. The introduction of Bragg grating in MIM WG can show the effect of the bandgap on the SPP waves. The coupling of the band-edge mode of SPP bandgap and the resonant mode of cavity/ring results in a proper resonance out of the entire structure which can be utilized for different applications like RI sensing. Such sensing structures are discussed in the following section.

4.3.2 Bragg Grating Structure–Based RI Sensors

One of the prominent architectures to generate the resonance by coupling effect between the WG and resonator is the Bragg grating model. In achieving the Bragg gratings in the plasmonic structures, the WG is etched in some way to generate the segments or bulging in the regular structure. The bulged shapes help in changing the effective RI of the WG. Such models have been reported as Bragg grating structures. The model is designed in such a way to fulfill the Bragg condition [99]:

$$d_1 \times \text{Real}(n_{\text{eff}1}) + d_2 \times \text{Real}(n_{\text{eff}2}) = \lambda_B/2 \quad (21)$$

where $n_{\text{eff}1}$ and $n_{\text{eff}2}$ are the effective refractive indices of the widest and narrowest parts of Bragg grating, d_1 and d_2 are the length of the two consecutive segments, and λ_B is the Bragg resonance wavelength. The segments are replicated periodically to shape the periodic MIM Bragg grating. The period number (N) is chosen wisely to decrease the loss because of robust metal absorption and to make the sensor compact. The optimized design parameters are of the MIM Bragg grating are $w_1 = 100 \text{ nm}$, $w_2 = 80 \text{ nm}$, $h = 100 \text{ nm}$, $d_1 = d_2 = 202 \text{ nm}$ and $N = 10$. With this, a highly sensitive RI sensor can be obtained, but still, the FoM is relatively lower which can be enhanced by introducing a nanocavity as reported in [111, 112]. An example of such a structure is shown in Fig. 11.

Figure 11 shows a potential construction with a Bragg grating and a side-linked nanocavity. The arrangement has made it easier to generate the Fano effect by interfering between a continuous state produced by the Bragg grating and a discrete state produced by the nanocavity. Furthermore, changing the make-ups regularly allows for unexpected manipulation of the Fano effects. As plasmonic sensors, many metallic nanostructures

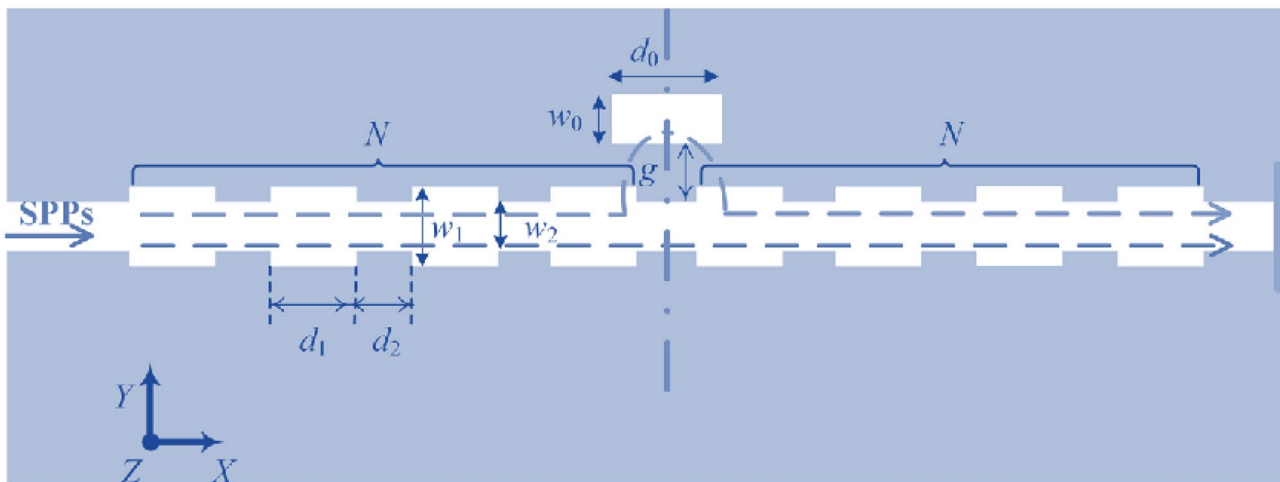


Fig. 11 Schematic of a Bragg grating and a nanocavity structure [111]. Dimensions of the structures are as follows: $w_1 = 100 \text{ nm}$, $w_2 = 80 \text{ nm}$, $d_1 = 202 \text{ nm}$, $d_2 = 202 \text{ nm}$, $w_0 = 80 \text{ nm}$, $d_0 = 520 \text{ nm}$, $g = 30 \text{ nm}$, and $N = 4$

based on gratings have been created and evaluated. Table 3 compares some of the recently developed plasmonics sensors based on metallic nanostructures with plasmonic Bragg grating based on MIM WG, their performances, and their applications.

Table 3 shows that the sensitivity of MIM sensors with Bragg grating is higher than that of plasmonic sensors based on metallic nanostructures in general. The FoM, on the other hand, is viewed in the opposite light. However, in the case of MIM plasmonic Bragg grating paired with MIM plasmonic nanocavity realizing prominent Fano resonance, both designs or configurations have large values. Moreover, Lorentzian resonances or Fano resonances are extremely sensitive to the change of RI in Bragg grating and nanoring cavities.

The other category of RI sensor is the temperature-dependent sensor. The primary concept of this category is the measurement of the ambient temperatures by observing the variations of RI of the temperature sensing element. This is described in the following section.

4.3.3 Temperature-Dependent Sensors

A device used to measure the temperature variation of gas, liquid, and solid is a temperature sensor. In plasmonic temperature sensors, some liquids are filled in the WG-resonator system. Once the working temperature of the system changes by some means, the RI of these liquids gets changed. For precisely measuring the temperature variation, the liquids used should have a high RI-temperature coefficient. With these inherent characters, the temperature sensors are designed.

As shown in Fig. 12, ethanol is filled in the WG and resonator system so that its RIs are changed from n_1 through n_n as an effect of temperature variation from T_1 to T_n and, consequently, the resonance shift in wavelengths occurs. Some of the aforementioned devices (Table 2) are also suitable for use as a nanoscale temperature sensor, with the RI change of the liquid being dependent on the change in effective temperature. The relationship between RI of the liquid dielectric layer to temperature can be evaluated as [103]

$$n = n_0 \frac{\Delta n}{\Delta T} (T - T_0) \quad (22)$$

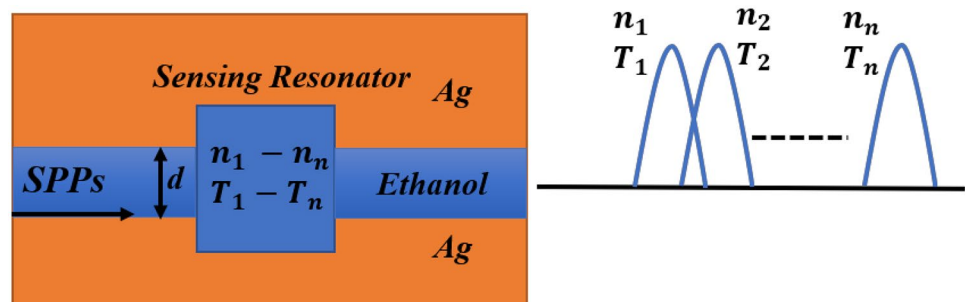
where T and n_0 are the environment or surrounding or local temperature to be known and the liquid's RI at the reference temperature (T_0) generally taken to be 20°C, respectively. $\frac{\Delta n}{\Delta T}$ is the temperature coefficient of RI of the liquid. As can be observed, the higher the $\frac{\Delta n}{\Delta T}$, the more sensitive the liquid is to temperature. Therefore, in a majority of the cases [90, 98, 100], it is discovered that ethanol is a suitable candidate for the dielectric layer due to its high RI coefficient (3.94×10^{-4}). The de-ionized water is the next option, as it has a high RI — temperature coefficient [103]. The temperature sensitivity of MIM plasmonic temperature-dependent sensors reported in the literature is compared in Table 4.

From Table 4, it has seemed that the temperature sensitivity is significantly large for the structure proposed in [100]. The structure is having two rectangular cavities (one is wider, and another is narrower) arranged in such a way to form the T-shaped cavity being coupled to the main bus WG. The device parameters are designated by different variables as can be reflected in Fig. 13. The T-shaped cavity is defected by adding the silver nanorods. The testing liquid (ethanol) is filled both in the bus WG and the cavity. By changing the temperature, the effective RI changes, and ultimately, the resonance wavelength changes as governed by Eq. (22) because the T-shaped cavity acts as a resonance source. The nanorod defect helps in confining the mode size in the nanometer scale. The device's radius of nanorods, as well as the length of the broader and narrower cavities, can be adjusted for optimizing the device.

4.3.4 Simultaneous Detection of RI and Temperature

Several plasmonic sensors based on MIM WG and SPP principles have been discussed in the previous sections. It can be observed that the sensitivities of these sensors are relatively high. However, they can be utilized for a single application like either to detect RI variations or temperature variations at an instance. In some testing labs, biological samples may require a controlled temperature setting in order to produce correct results. As a result, a lab-on-chip solution that can evaluate analytes and temperature at the same time is required. Recently, the MIM-based structures have also

Fig. 12 Block diagram of a plasmonic temperature sensor and corresponding wavelength shift



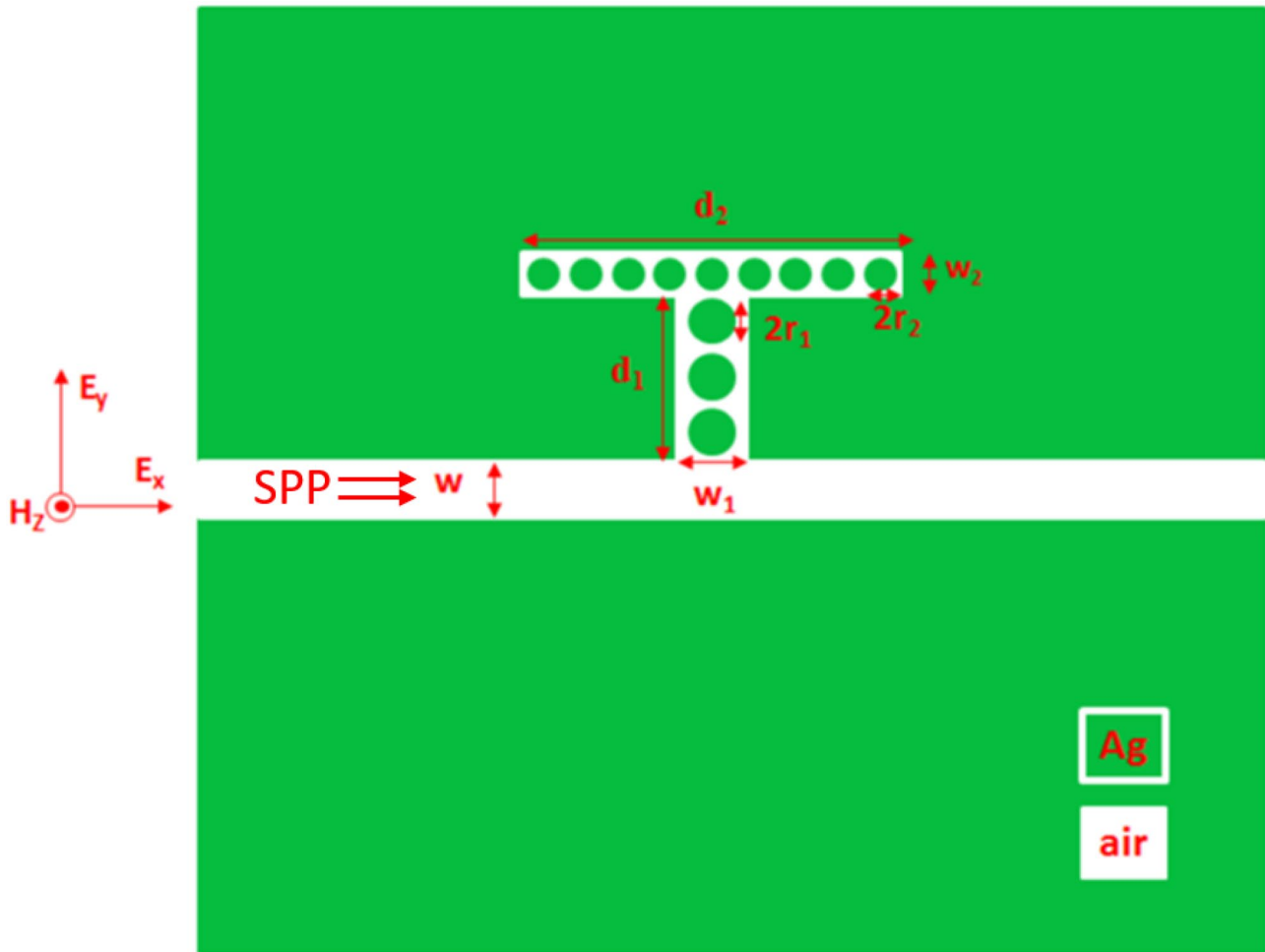


Fig. 13 MIM sensor construction with nanorod placed in T-shaped cavity shown schematically [100]. Dimensions of the structures are as follows: $w = 50\text{nm}$, $w_1 = 50\text{nm}$, $w_2 = 30\text{nm}$, $d_1 = 150\text{nm}$, $d_2 = 330\text{nm}$, $r_1 = 20\text{nm}$, and $r_2 = 10\text{nm}$

been designed to have multipurpose sensing applications simultaneously. With the commencement of multipurpose sensing abilities in a single design, it is quite possible to realize a multipurpose compact lab-on-chip sensor. An example of such a design that simultaneously acts as a biosensor to detect the RI changes of an analyte and a temperature sensor to detect the ambient temperature is proposed in [120].

As shown in Fig. 14, the structure consists of a MIM WG side coupled with two simple resonant cavities of square and circular shape. Of the two cavities, the square cavity is filled with an analyte to act as a biosensor and the circular cavity is filled with a thermo-optic polymer named polydimethylsiloxane, which provides a resonant shift with the variations of ambient temperature. Both sensing phenomena are independent of each other. The maximum RI sensitivity and temperature sensitivity achieved were $700\text{nm}/\text{RIU}$ and $-0.35\text{nm}/^\circ\text{C}$, respectively. The proposed sensor can be useful in two scenarios: (i) when measuring biological analytes

in a controlled temperature environment is required and (ii) when decreasing the impact of ambient temperature changes on real-time refractometric readings.

In the SPWG-based structures giving rise to Lorentzian profiles, the sensing ability of the sensor, in general, has been evaluated by calculating the sensitivity. Some of the sensors have been evaluated by calculating the sensitivity and FoM both. In addition to them, they need to be evaluated based on parameters like sensitivity, FoM, and Q -factor before they are realized at the operational level. Since the latter two factors (FoM and Q -factor) ensure the level of device optical resolution and losses, the higher the FoM value, the higher the optical resolution of the sensor, and the higher the Q -factor, the lower the losses. To get out of these operational level problems encountered in SPWG-based sensors, the HPWG-based sensors have been put forward. The explanation of the hybrid mode-based RI sensors is done in the next section.

4.4 Hybrid Plasmonic–Based Ring Resonator Structures for RI Sensing

For effectively evaluating hybrid plasmonic RI sensors, the focus must be on S , the FoM, and Q -factor. The proportion of resonant wavelength to full-wave at half maximum (FWHM) defines the Q -factor, i.e., $Q = \frac{\lambda_{\text{res}}}{\text{FWHM}}$. The laser beam in the main WG vanishingly couples with the ring in the microring resonator–hybrid plasmonic WG system, creating resonant modes at specific wavelengths. At this wavelength (λ_{res}), the output power transmission curve shows Lorentzian dips, which can be described by the following relationship [64].

$$\lambda_{\text{res}} = n_{\text{eff}} \frac{2\lambda R + 2L}{m} \quad (23)$$

where n_{eff} is the effective RI, L is the coupling distance, R is the ring radius, and m is an integer.

In Table 5, the performances of an HPWG linked with a ring resonator differently to act as a RI sensor are compared. The WG geometry is observed to play a critical role in mode confinement and lowering propagation loss. The majority of the structures are made of Au. The Q -factor for a hybrid WG ring resonator consisting of slot and stripe WGs is maximum because this construction combines slot WG with a low loss and strongly directed stripe WG into a single ring [121]. The Q -factor for hybrid plasmonic WG structures was measured between 70 and 18,500.

The results of Tables 2, 3, and 5 show that the values of FoM of RI sensors based on plasmonic resonator, Bragg grating, and hybrid plasmonic resonator are relatively lower because of their Lorentzian line like resonances which are symmetrical and wider in bandwidth. Their values lie between some tens to a few hundred. From the Tables, it is seen that the FoMs can be enhanced by utilizing the Fano effects both on the Bragg grating structures [111] and plasmonic resonating structures [76] because Fano peaks/dips are sharper and narrower than the Lorentzian counterparts. However, the Q -factor has not been taken into consideration in these sensors. Mostly, the Q -factor is considered and calculated in the case of HPWG-based structures. For practical realization, all these three parameters need to be calculated.

Based on the surveyed results in terms of performance parameters of the sensors, the evolution of prominent structures based on SPWG and HPWG is explored in the following section.

5 Evolution of Recently Reported Sensors and Challenges

Several MIM-resonator systems have recently been put forward and researched for sensing utilities, as shown in Tables 2–5. Lorentzian line forms can be seen in some recent SPWG-based sensors, but sharp Fano peaks can be seen in others. Even while simple plasmonic sensors are

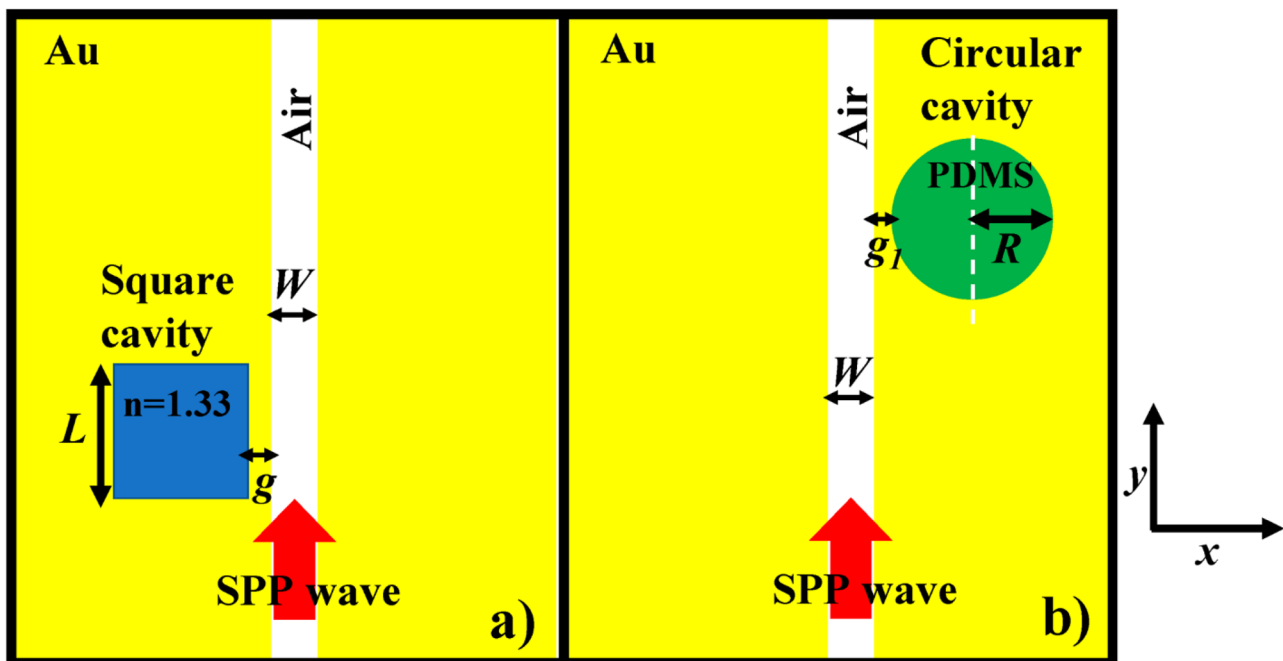


Fig. 14 Schematic top view of the plasmonic cavity side coupled to MIM WG. (a) Square cavity filled with dielectric medium and (b) circular cavity filled with thermo-optic material; polydimethylsi-

loxane (PDMS) [120]. Dimensions of the structures are as follows: $W = 50\text{nm}$, $L = 280\text{nm}$, $R = 340\text{nm}$, $g = 20\text{nm}$, and $g_1 = 10\text{nm}$

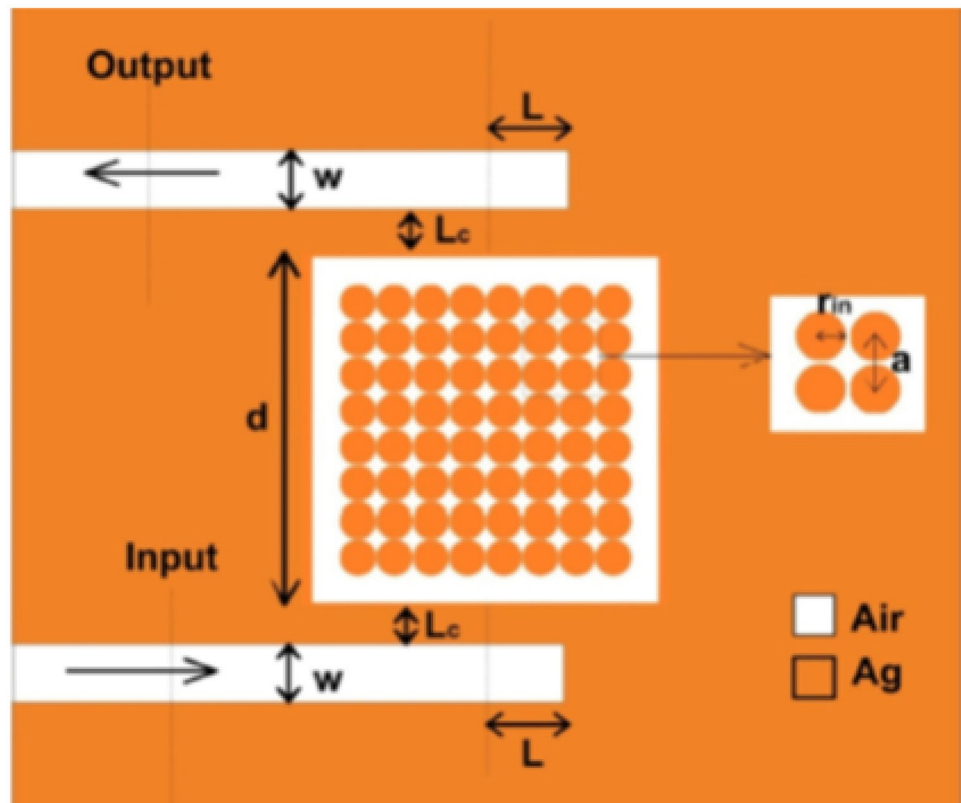
compact and easy to incorporate on-chip, and their sensitivity can be increased with structural modifications, their FoM is not as high as Fano plasmonic sensors, as shown in [67]. Moreover, the Q -factor which signifies the accuracy and efficiency of the plasmonic sensor has not been the subject of study in SPWG-based sensors that generate Lorentzian line shape. Hence, bringing the proper balance between the sensitivity and FoM of plasmonic sensors is to enhance the Q -factor which is a challenge and a pivot area of research in the field of plasmonic sensors. This challenge can be best viewed by reviewing the latest models and their performances. A quick assessment of structures with a sensitivity of greater than 1000 nm/RIU was carried out as follows: Butt et al. presented an edge connected SRR with S and FoM maximums of 1367 nm/RIU and 25 RIU⁻¹, respectively [68]. Rakhshani et al. [70] proposed a novel design shown in Fig. 15 that comprises two MIM WGs sides coupled with a square cavity filled with silver nanorods. Nanorods are utilized to take advantage of their unique optical features, such as nanoscale confinement and reduced propagation losses. Moreover, the main advantage offered by the square cavity resonator as compared to the ring and disk resonator is that it helps in fixing a separation gap between the resonator and the side-coupled WG. The design can be optimally tweaked by altering the side length of the square cavity and the radius of the nanorods,

and it can deliver the best sensitivity of 2320 nm/RIU with the aforementioned practical advantages [70].

Luo et al. [84] described a plasmonic MIM WG linked dual cavity structure with a rectangle and a disk as side linked cavities achieving S and FoM of 1136 nm/RIU and 51,275/RIU, respectively. Designers are attempting to improve resonators by improving S , the proportion of transmittance spectrum fluctuations, and structural dimensions, all of which affect the sensor's quality and accuracy. Rahmatiyar et al. [65] developed a unique design consisting of a defective MIM WG paired with a defective ring resonator, which obtained a good S of 1295 nm/RIU and a maximum FoM of 159.67 /RIU, as shown in Fig. 16. The tunability is assured by modulating the WG and ring through the presence or lack of tapering defects. The performance is evaluated by varying the radius of the ring. The designs demonstrated that adding tapered periodic defects to the WG enhances the proportion of the transmission spectrum, whereas adding defects to the ring resonator causes resonance positions to vary. By combining these two advantages, the FoM can be greatly enhanced with an acceptable sensitivity value.

Zhang et al. [85] proposed and numerically evaluated a plasmonic RI sensor based on a MIM WG side linked with two co-centered rings resonators. Super modes were a unique aspect of the sensor's transmission spectrum. The

Fig. 15 Two MIM WGs are shown side by side, each with a square cavity filled with silver nanorods [70]. Dimensions of the structures are as follows: $w = 50\text{nm}$, $L_c = 15\text{nm}$, $L = 40\text{nm}$, $d = 380\text{nm}$, $r = 0.5\text{nm}$, and $a = 40\text{nm}$



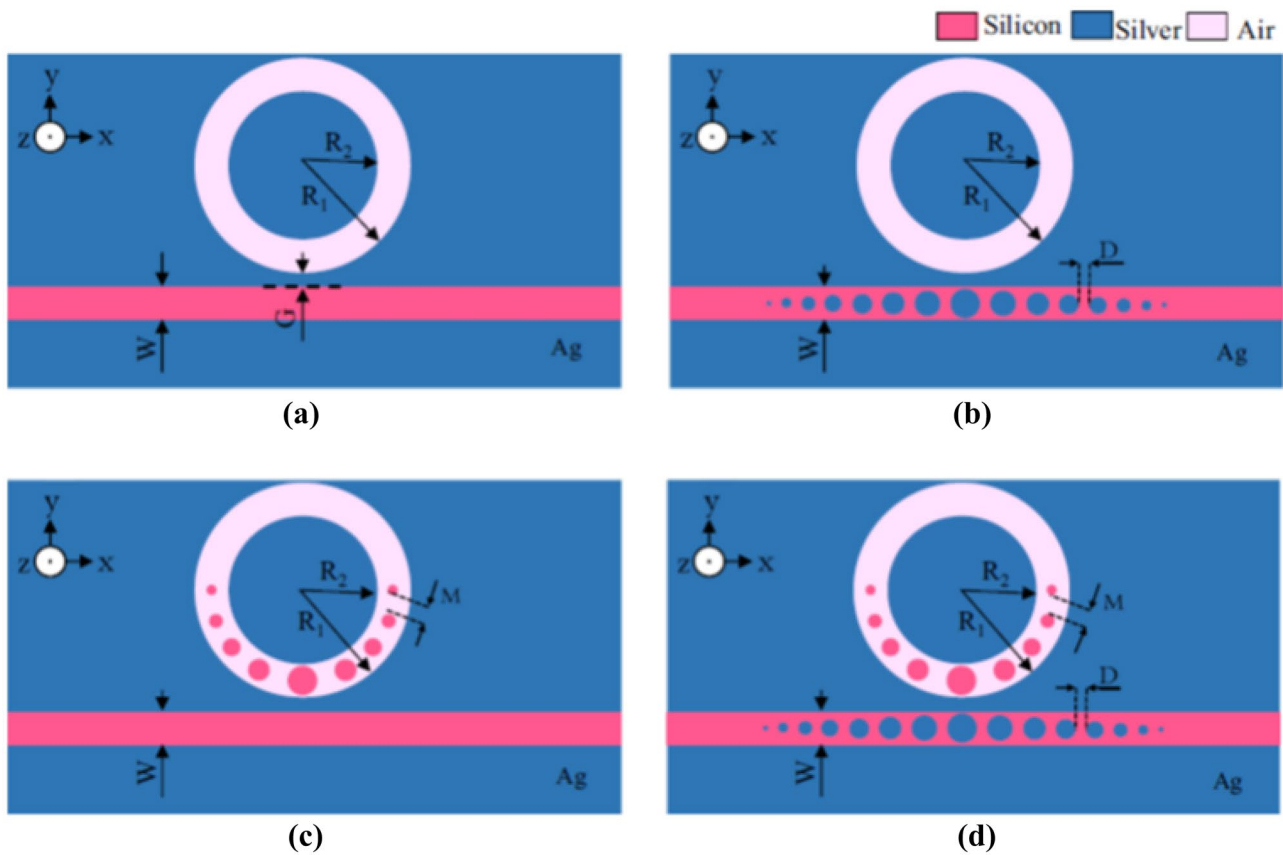


Fig. 16 Schematic diagram (a) a MIM WG side coupled ring resonator, (b) a defected MIM WG side coupled with a ring resonator, (c) a MIM WG side coupled with a defected ring resonator, and (d) both WG and ring resonator having defects [65]. Dimensions of the structures are as follows:

$w = 100\text{nm}$, $G = 15\text{nm}$, $D = 250\text{nm}$, $M = 22.5^\circ$, $R_1 = 350\text{nm}$, and $R_2 = 250\text{nm}$. The defects are with the radius of 40, 35, 30, 25, 20, 15, 10, and 5nm

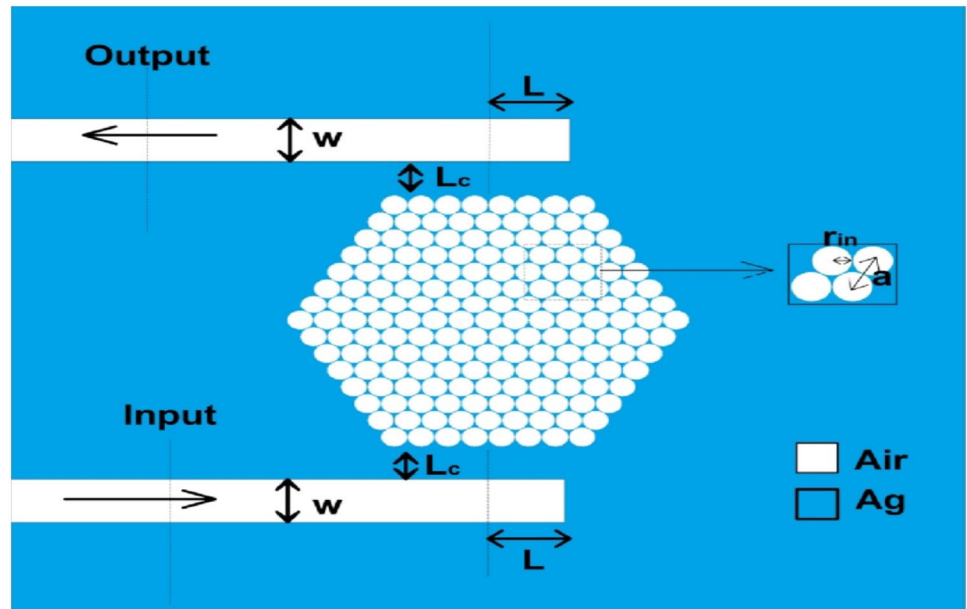
super modes indicate that both the inner and outer rings are in resonance at the same time. There are only two types of super modes: antiphase in the inner ring when the energy is mostly trapped in the outer ring, and phase in the inner ring when the energy is mostly trapped in the inner ring. This sensor's sensitivity and FoM are 1060 nm/RIU and 203.8, respectively. Rakhshani et al. [89] proposed a structure that comprises two MIM WGs side coupled to a hexagonal array of nanoholes as a resonator which is shown in Fig. 17. The proposed design has two functional structures—one is a hexagonal cavity, and the other one is an array of nanoholes. The former reduces the radiation loss of SPP propagation, increasing sensitivity even further. Long side interaction in the hexagonal resonator can effectively reduce a lot of limits on the spacing between the WG and the resonator. Nanoholes are more mechanically strong than nanorods, and they are less delicate and readily split. The nanohole arrays have a high extinction and scattering coefficient, which is critical for efficiently sensing chemicals and biological materials. The proposed design has been adjusted to acquire the best optical property of nanoholes by simply modifying parameters

such as metal thickness, array periodicity, and nanohole radii, resulting in a maximum sensitivity of 3172 nm/RIU [89].

Rakhshani et al. [90] reported a RI sensor using a symmetrically side coupled hexagonal ring between two MIM WGs as shown in Fig. 18 in which the value of sensitivity is 4270 nm/RIU and the value of FoM is 37. The hexagonal cavity collects electromagnetic energy from the input and sends it to the output. The hexagonal cavity offers three unique features such as high Q , inherent single-mode, and substantial light confinement; it behaves as a RI detector of the matter placed within it. The length effectiveness, which is the mean of the radii of the interior and exterior rings of the hexagonal ring resonator, can be changed to tailor the construction. Furthermore, increasing the inner radius of the ring improves sensitivity [90].

Mahmud et al. proposed a RI sensor using an edge coupled equilateral triangular resonator with a MIM straight WG in which the achieved sensitivity was 2713 nm/RIU and FoM was 35.1 with sensing resolution as high as 3.68×10^{-6} . The equilateral triangle has been placed in two configurations [93]: first as a disc resonator and second

Fig. 17 The schematic diagram of the sensor structure having two MIM WG sides coupled to an array of hexagonal nanoholes [89]. Dimensions of the structures are as follows: $w = 50nm$, $L_c = 15nm$, $L = 40nm$, $r_{in} = 0.5nm$, and $a = 40nm$

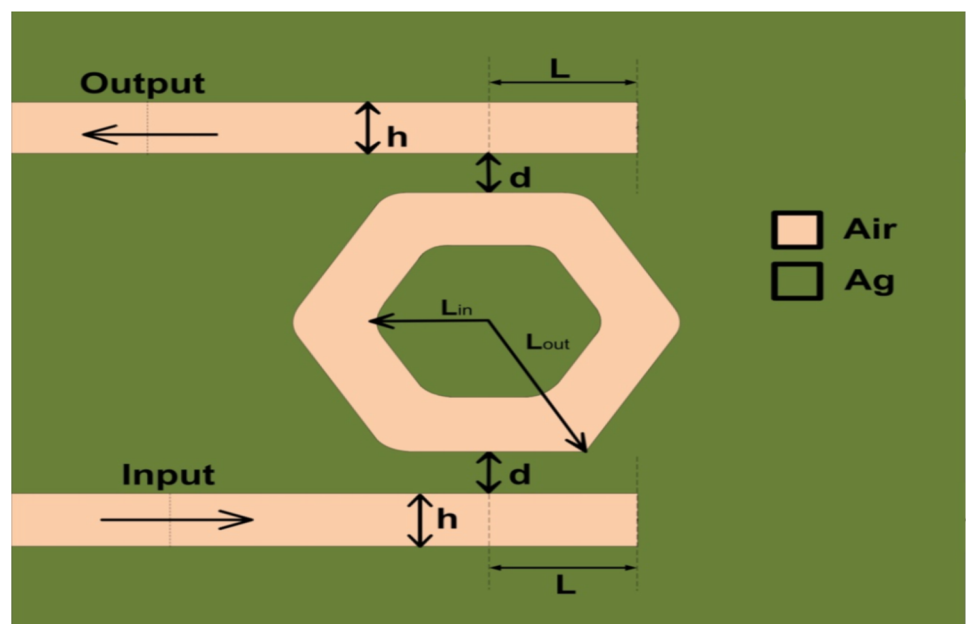


as a ring resonator. There is just one interface between the metal–insulator and the ring in the former design, whereas there are two interfaces on both sides of the ring in the latter configuration. This aids in the propagation of more SPPs in the latter instance, resulting in more field augmentation and confinement, ultimately contributing to the device’s increased sensitivity. Rakhshani et al. [103] built a plasmonic sensor with a racetrack resonator side coupled with the two MIM WGs as pictured in Fig. 19(a and b) to magnify the coupling efficiency of such plasmonic structures. When compared to traditional ring and disc resonators, it has a longer edgewise interplay distance over the complete

outstretched resonator sidewalls, substantially relieving the tight constraint or separation between the resonator and the disc connected WG [103]. The highest S and FoM reported were 4650 nm/RIU and 37, respectively. The racetrack resonator’s inner radius is changed to tune the device.

The resonator is filled with the material to be sensed, and the RI changes induce a swift in the wavelength of the exit passage. Butt et al. presented a MIM square ring resonator with an array of nanodots (NDs) on all four sides of the cavity to boost the sensor’s sensitivity. Because the NDs behave as metallic grating, they aid in the intensification of the SPPs [71]. The ring resonator is subject to ambient RI with this

Fig. 18 Schematic showing plasmonic sensor having two MIM WGs optically connected to a hexagonal ring resonator [90]. Dimensions of the structures are as follows: $h = 50nm$, $d = 15nm$, $L = 40nm$, and $L_{avg} = \left(\frac{L_{in}+L_{out}}{2}\right) = 165nm$



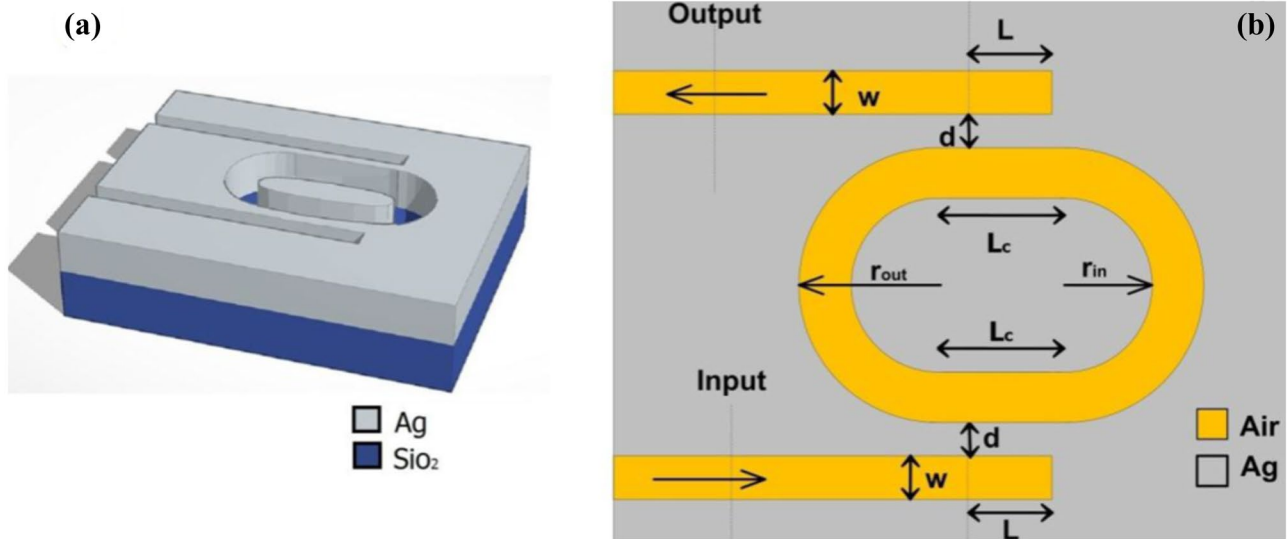


Fig. 19 (a) 3-D schematic and (b) top view of a plasmonic sensor having two MIM WGs side coupled with the racetrack resonator [103]. Dimensions of the structures are as follows: $d = 15\text{nm}$, $r = 150\text{nm}$, $L = 40\text{nm}$, $L_c = 120\text{nm}$, and $w = 50\text{nm}$

new property of NDs, and the resonance wavelength redshifts with rising RI. The maximal sensitivity, FoM, and Q -factor of the design are 1240 nm/RIU , 20, and 20.9. Butt et al. [105] proposed a bow tie cavity resonator–based plasmonic sensor. They pioneered the use of a nanowall in the bow tie cavity design to achieve a sensitivity of 2300 nm/RIU as a result of powerful SPP mode trapping in the small zone and high light–matter interaction [105]. The reported maximum FoM and Q -factor are 31.5 and 31.1, respectively. The three different concepts of bow tie configurations are shown in Fig. 20(a–c), where the first configuration has only bow tie cavity side coupled to the main WG, the second configuration consists of nanorods incorporated by flattening the V—the

shape of the bow tie, and the third configuration consist of nanowalls. The performance of these schemes is compared which clearly shows that the sensitivities of the schemes that incorporated the nanodot or nanowall outwit the standard bow tie configuration. The nanodots play a critical function in the amplification of E-field within the cavity’s small zone. The size and number of nanorods and nanowalls perform a vital part in the effective execution of the device.

The novel design proposed by Kazanskiy et al. is a RI sensor that embodies a semi-ring cavity with decorated gold nanodots and without nanodots (standard semi-ring) edge coupled to a MIM WG. The standard semi-ring resonator offer sensitivity of 600 nm/RIU . The cavity filled with nanodots, on the other

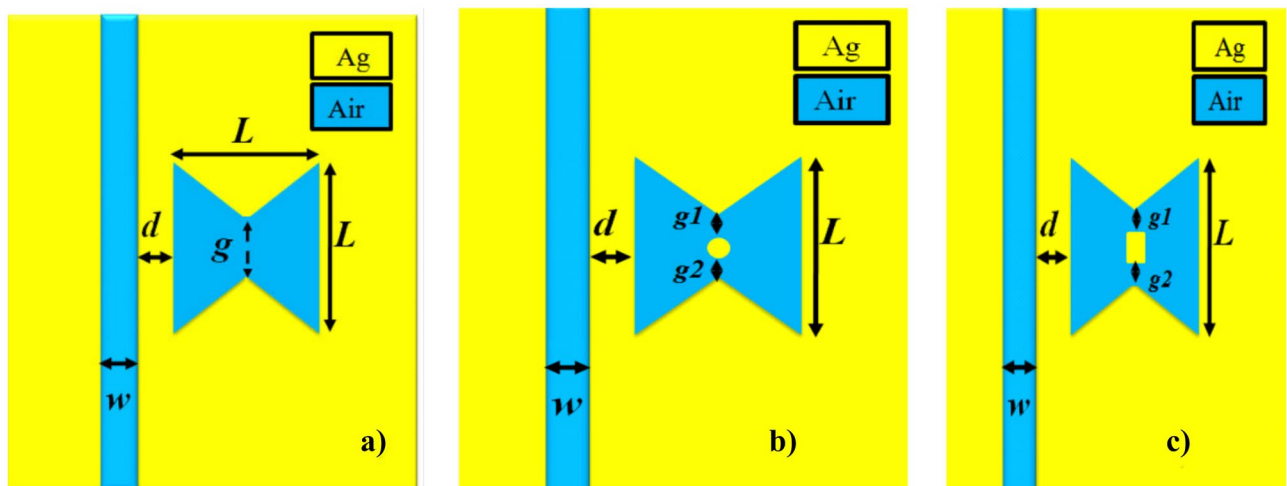


Fig. 20 Sensor schematic (a) standard bow tie scheme, (b) nanodot incorporated bow tie scheme, and (c) nanowall incorporated bow tie scheme [105]. Dimensions of the structures are as follows: $w = 50\text{nm}$, $L = 350\text{nm}$, $d = 30\text{nm}$, $g = 30\text{nm}$, $g_1 = 5\text{nm}$, and $g_2 = 5\text{nm}$

hand, aids in the amplification of resonant SPPs mode [106]. In comparison to a normal semi-ring design, this design has been shown to enhance and deliver a high S of 1084.21 nm/RIU as a result of strong light–matter interaction. The FoM and Q -factor, respectively, are 157.89 and 167.89. The above-discussed structures have shown good figures for S , but the majority of them show lesser FoM and Q -factor. The recent structures that are based on the HPWG platform are candidates to simultaneously enhance all these performance measures.

Some of the most modern sensors based on HPWGs and ring resonators are, therefore, discussed. Butt et al. presented an HPWG geometry made up of a microracetrack ring and a straight bus WG. Based on two modes i.e., dielectric mode and hybrid mode, two configurations are studied for RI sensing applications. Both modes have a confinement factor for TE and TM polarization of above 65% with minimal propagation losses when this design is optimized [64]. The maximum S for dielectric mode is 200 nm/RIU in configuration I, whereas the S for hybrid mode is 230 nm/RIU in configuration II. Sun et al. proposed an a-Si bud WG side coupled with a double slot hybrid plasmonic ring with an S of 687.5 nm/RIU [123]. Steglich et al. demonstrated a hybrid WG ring resonator with an S of 106.29 nm/RIU, FoM of 1337, and a Q -factor of 18,500 using a typical silicon slot and stripe WG [121]. Butt et al. demonstrated a MIM microring resonator with an integrated hybrid plasmonic

WG. As a consequence of substantial overlay between the hybrid mode–SPP mode and the analytes, mutual interaction between the photonic mode in the silicon WG and the plasmonic mode at the metal surface results in a high sensitivity [124]. With an FoM of 37, the best S of 800 nm/RIU was achieved. Butt et al. proposed a new design that combines a hybrid plasmonic WG side with a ring resonator to achieve the best S of 1000 nm/RIU [125].

Both SPWG- and HPWG-based RI sensors, after theoretical validation, are taken for fabrication. If their theoretical results resemble that of fabrication results, then they can be a part of real-time applications as lab-on-chip. So, it is assumed meaningful to state the prominent fabrication schemes in the immediate section.

6 Fabrication Realization

Many of the structures were designed and analyzed numerically. To validate the theoretical investigation, some of the structures are realized through fabrication procedure. The most widely used fabrication techniques include electron beam lithography (EBL) [120], focused ion beam milling (FIB), deep-UV projection lithography, and nanoimprint lithography (NIL) [128]. Even though the first three varieties are time-consuming and costly to mass product, they have

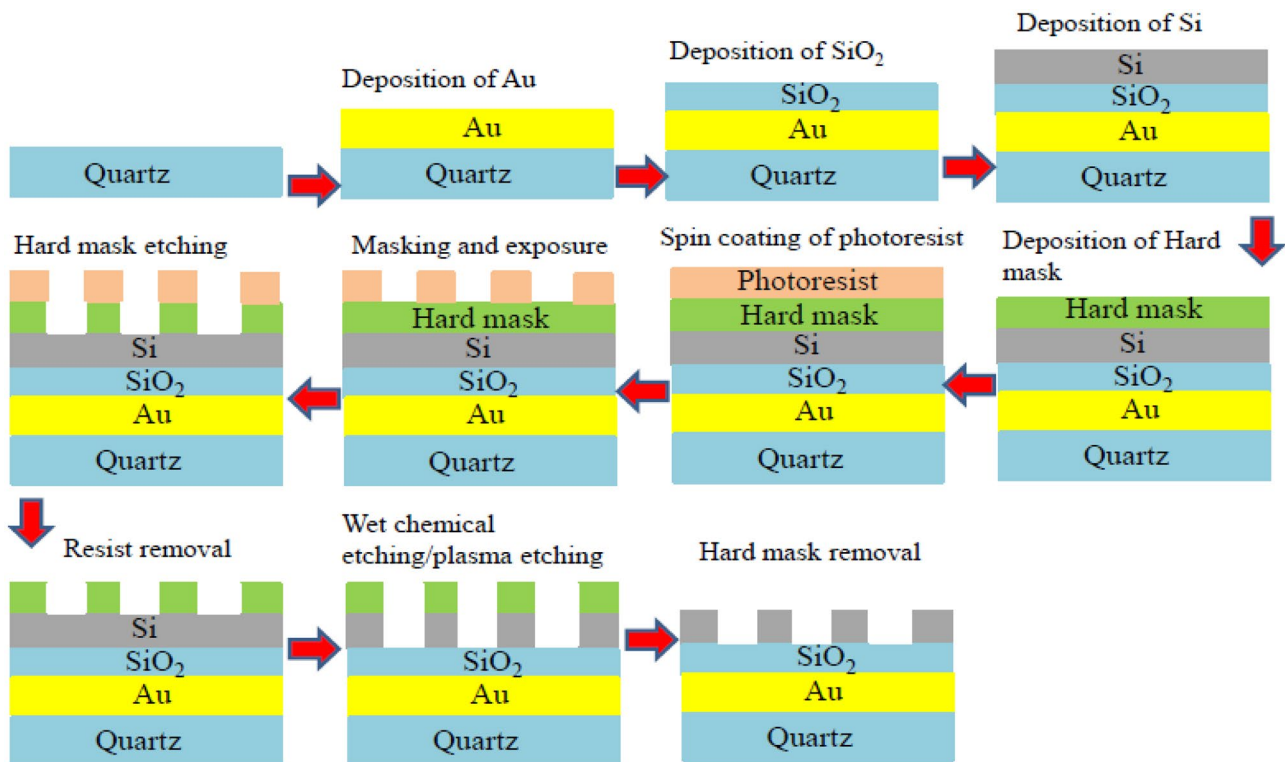


Fig. 21 The fabrication steps of the silicon stripe WG ring resonator by [122]

not been completely displaced by the most recent ones. For mass production with greater throughput and resolution at minimum cost, the NIL approach can be used. A fine coating of Ag is dumped on a silica substratum, accompanied by EBL decorating the layout for the manufacture of plasmonic WG-based sensors. Then, to realize the MIM WGs, a chemical etching (nitric acid and water) phenomenon was used on the undesired regions of the Ag. The FIB approach and EBL can be used to build the racetrack resonator-based MIM plasmonic sensor suggested by [103]. As the hybrid plasmonic WG, for instance, silicon stripe ring resonator [121] can be fabricated by adopting the following process. A SiG BiCMOS pilot line is used. A grating coupler setup was used for optical characterization. Similarly, a highly sensitive sensor with a dual-slot hybrid plasmonic resonator was built in [123] as follows: manufacture begins with an SOI wafer with Si on the crest of a SiO₂ buffer surface. The Si structure is patterned with EBL.

Then, EBL is followed by an inductively coupled plasma (ICP) dry etching operation. Finally, the third E-beam exposure introduces the pattern of the Ag pads. Next, the optical characterization was done by grating coupler setup. The fabrication steps of the silicon strip WG ring resonator are orderly illustrated in Fig. 21. For more theoretical and practical guidelines for fabricating the simple plasmonic as well as hybrid plasmonic WG-based sensors and more other architectures, it is suggested to refer to [129].

7 Conclusions and Future Directions

Because the optical sensor is such a vast issue, we concentrated on recent advances in sensors that detect changes in the RI using a simple plasmonic MIM WG and a hybrid plasmonic WG. We also mentioned some notable structures based on simple plasmonic MIM WGs as temperature-dependent sensors for monitoring changes in ambient liquid (ethanol or deionized water) temperature. Materials and their models, as well as interrogation tactics, were also included in this review. This work mostly focused on sensors that were constructed and examined theoretically and quantitatively. Only ring, cavity, or Bragg grating sensors were surveyed. These innovative designs' spectral properties and electric field distribution were investigated using either the finite element method or the finite difference time domain method. The designed sensors are compared in tabulated form based on performance metrics such as sensitivity, a figure of merit, and Q -factor (which is especially beneficial in the case of hybrid plasmonic-based design). The huge line width in the transmission profile under the resonance situation is one of the most important concerns in plasmonics. This is due to the enormous radiation dampening of the metallic layers, which lowers FoM and Q -factor. FoM is the

most generic benchmark for contrasting the accomplishment of plasmonic-based sensors, in addition to sensitivity.

Unlike dielectric WGs, where propagation losses are negligible, plasmonic WGs suffer from high losses due to the existence of metals as guiding layers. WG-based structures are typically intended to strike a balance between propagation loss and mode imprisonment. Moreover, hybrid plasmonic WG-based layouts compromise the merits offered by both dielectric WGs and plasmonic WGs so that they offer high mode confinement and low propagation loss. Several plasmonic resonator designs were mentioned, with maximum sensitivity ranging from 685 to 8283 nm/RIU. Several plasmonic Bragg grating configurations were proposed, with extraordinarily good sensitivity ranging from 190 nm/RIU to as high as 1960 nm/RIU. Numerous resonator layouts were mentioned that have exceptionally high-temperature sensitivity ranging from -0.53 to 3.30 nm/°C. Various hybrid plasmonic resonator architectures were reported, with sensitivity ranging from 106.7 to 1000 nm/RIU and Q -factor ranging from 70 to 18,500.

Because of its interoperability with existing CMOS microelectronics technologies during manufacture, silicon-based hybrid plasmonic WG architectures have piqued interest and will continue to do so for many years. The field of plasmonics and its hybrid version is anticipated to continue to govern the studies and improvements of blended optical circuits used in communication, computer warehouse, sensing, and digital image processing, thanks to significant noteworthy explorations based on surface plasmon waveguiding and lossless propagation waveguiding in sub-wavelength regimes.

Declarations

Conflict of interest The authors declare no competing interests.

References

1. P.R. West, S. Ishii, G.V. Naik, N.K. Emani, V.M. Shalaev, A. Boltasseva, Searching for better plasmonic materials. *Laser Photonics Rev.* **4**(6), 795–808 (2010). <https://doi.org/10.1002/lpor.200900055>
2. Y. Chen, H. Ming, Review of surface plasmon resonance and localized surface plasmon resonance sensor? *Photonic Sensors* **2**(1), 37–49 (2012). <https://doi.org/10.1007/s13320-011-0051-2>
3. W.L. Barnes, A. Dereux, T.W. Ebbesen, Surface plasmon sub-wavelength optics. *Nature* **424**(6950), 824–830 (2003). <https://doi.org/10.1038/nature01937>
4. S.E. Swiontek, D.P. Pulsifer, A. Lakhtakia, Optical sensing of analytes in aqueous solutions with a multiple surface-plasmon-polariton-wave platform. *Sci. Rep.* **3**(1), 1–6 (2013). <https://doi.org/10.1038/srep01409>
5. Y. Fang, M. Sun, Nanoplasmonic waveguides: towards applications in integrated nanophotonic circuits. *Light Sci. Appl.* **4**(6), e294–e294 (2015). <https://doi.org/10.1038/lsa.2015.67>

6. P.K. Skorobogatov, Laser imitation simulation behind the diffraction limit. *Russ. Microelectron.* **43**(2), 125–132 (2014). <https://doi.org/10.1134/S1063739714020097>
7. X. Luo, L. Yan, Surface plasmon polaritons and its applications. *IEEE Photonics J.* **4**(2), 590–595 (2012). <https://doi.org/10.1109/JPHOT.2012.2189436>
8. J. Zhang, L. Zhang, W. Xu, Surface plasmon polaritons: physics and applications. *J. Phys. D. Appl. Phys.* **45**(11), (2012). <https://doi.org/10.1088/0022-3727/45/11/113001>.
9. S.H. Abdulnabi, All-optical logic gates based on nanoring insulator–metal–insulator plasmonic waveguides at optical communications band. *J. Nanophotonics* **13**(01), 1 (2019). <https://doi.org/10.1117/1.jnp.13.016009>
10. J.S. Costa et al., Limits of the effective medium theory in particle amplified surface plasmon resonance spectroscopy biosensors. *Sensors (Switzerland)* **19**(3), 1–17 (2019). <https://doi.org/10.3390/s19030584>
11. M.-S. Kwon, Metal-insulator-silicon-insulator-metal waveguides compatible with standard CMOS technology. *Opt. Express* **19**(9), 8379 (2011). <https://doi.org/10.1364/oe.19.008379>
12. Q. Zaman et al., Dielectric-loaded waveguides as advanced platforms for diagnostics and application of transparent thin films. *Langmuir* **37**(11), 3248–3260 (2021). <https://doi.org/10.1021/acs.langmuir.0c02862>
13. R. El Haffar, A. Farkhsi, and O. Mahboub, Optical properties of MIM plasmonic waveguide with an elliptical cavity resonator. *Appl. Phys. A Mater. Sci. Process.* **126**(7), (2020). <https://doi.org/10.1007/s00339-020-03660-w>.
14. Y. Jin Zhou, X. X. Yang, and T. Jun Cui, A multidirectional frequency splitter with band-stop plasmonic filters. *J. Appl. Phys.* **115**(12), 11–16 2014. <https://doi.org/10.1063/1.4870135>.
15. Y. Guo et al., A plasmonic splitter based on slot cavity. *Opt. Express* **19**(15), 13831 (2011). <https://doi.org/10.1364/oe.19.013831>
16. Z. Zhang, F. Shi, Y. Chen, Tunable multichannel plasmonic filter based on coupling-induced mode splitting. *Plasmonics* **10**(1), 139–144 (2015). <https://doi.org/10.1007/s11468-014-9787-z>
17. X.-S. Lin, X.-G. Huang, Tooth-shaped plasmonic waveguide filters with nanometric sizes. *Opt. Lett.* **33**(23), 2874 (2008). <https://doi.org/10.1364/ol.33.002874>
18. J. Tao, X.G. Huang, X. Lin, Q. Zhang, X. Jin, A narrow-band subwavelength plasmonic waveguide filter with asymmetrical multiple-teeth-shaped structure. *Opt. Express* **17**(16), 13989 (2009). <https://doi.org/10.1364/oe.17.013989>
19. J. Xu, L. Chen, X. Zang, B. Cai, Y. Peng, Y. Zhu, Triple-channel terahertz filter based on mode coupling of cavities resonance system. *Appl. Phys. Lett.* **103**(16), 2–6 (2013). <https://doi.org/10.1063/1.4826456>
20. D. Chauhan, A. Kumar, R. Adhikari, R. K. Saini, S. H. Chang, and R. P. Dwivedi, High performance vanadium dioxide based active nano plasmonic filter and switch. *Optik (Stuttg)* **225**, 165672 (2021). <https://doi.org/10.1016/j.ijleo.2020.165672>.
21. Y. Kou, X. Chen, Multimode interference demultiplexers and splitters in metal-insulator-metal waveguides. *Opt. Express* **19**(7), 6042 (2011). <https://doi.org/10.1364/oe.19.006042>
22. H. Lu, X. Liu, Y. Gong, D. Mao, G. Wang, Analysis of nanoplasmonic wavelength demultiplexing based on metal-insulator-metal waveguides. *J. Opt. Soc. Am. B* **28**(7), 1616 (2011). <https://doi.org/10.1364/josab.28.001616>
23. K. Wen, L. Yan, W. Pan, B. Luo, Z. Guo, and Y. Guo, Wavelength demultiplexing structure based on a plasmonic metal-insulator-metal waveguide. *J. Opt. (United Kingdom)* **14**(7), (2012). <https://doi.org/10.1088/2040-8978/14/7/075001>.
24. M. Bahadori, A. Eshaghian, H. Hodaei, M. Rezaei, K. Mehrany, Analysis and design of optical demultiplexer based on arrayed plasmonic slot cavities: transmission line model. *IEEE Photonics Technol. Lett.* **25**(8), 784–786 (2013). <https://doi.org/10.1109/LPT.2013.2250951>
25. Z. Chen, R. Hu, L. Cui, L. Yu, L. Wang, J. Xiao, Plasmonic wavelength demultiplexers based on tunable Fano resonance in coupled-resonator systems. *Opt. Commun.* **320**, 6–11 (2014). <https://doi.org/10.1016/j.optcom.2013.12.079>
26. R.A. Wahsheh, Z. Lu, M.A.G. Abushagur, Nanoplasmonic couplers and splitters. *Opt. Express* **17**(21), 19033 (2009). <https://doi.org/10.1364/oe.17.019033>
27. A. R. Davoyan, Plasmonic couplers with metal nonlinearities. *Phys. Lett. Sect. A Gen. At. Solid State Phys.* **375**(14), 1615–1618 2011. <https://doi.org/10.1016/j.physleta.2011.03.001>.
28. H.Y. Wu et al., Ultrasmall all-optical plasmonic switch and its application to superresolution imaging. *Sci. Rep.* **6**(April), 1–9 (2016). <https://doi.org/10.1038/srep24293>
29. R.P. Dwivedi, H.S. Lee, J.H. Song, S. An, E.H. Lee, Plasmonic modulator utilizing three parallel metal-dielectric-metal waveguide directional coupler and elasto-optic effects. *Opt. Commun.* **284**(5), 1418–1423 (2011). <https://doi.org/10.1016/j.optcom.2010.10.038>
30. V.E. Babicheva et al., Towards CMOS-compatible nanophotonics: ultra-compact modulators using alternative plasmonic materials. *Opt. Express* **21**(22), 27326 (2013). <https://doi.org/10.1364/oe.21.027326>
31. D. Chauhan, G. T. Mola, and R. P. Dwivedi, An ultra-compact plasmonic modulator/switch using VO₂ and elasto-optic effect. *Optik (Stuttg)* **201**, 163531 2020. <https://doi.org/10.1016/j.ijleo.2019.163531>.
32. J. Chen, Z. Li, Y. Zou, Z. Deng, J. Xiao, Q. Gong, Coupled-resonator-induced Fano resonances for plasmonic sensing with ultra-high figure of merits. *Plasmonics* **8**(4), 1627–1631 (2013). <https://doi.org/10.1007/s11468-013-9580-4>
33. Zhao, L. Yu, L. Wang, G. Duan, Y. Zhao, and J. Xiao, A refractive index nanosensor based on fano resonance in the plasmonic waveguide system. *IEEE Photonics Technol. Lett.* **27**(16), 1695–1698 2015. <https://doi.org/10.1109/LPT.2015.2437850>.
34. Y. Zhang et al., Evolution of Fano resonance based on symmetric/asymmetric plasmonic waveguide system and its application in nanosensor. *Opt. Commun.* **370**, 203–208 (2016). <https://doi.org/10.1016/j.optcom.2016.03.001>
35. Y. Tang et al., Refractive index sensor based on fano resonances in metal-insulator-metal waveguides coupled with resonators. *Sensors (Switzerland)* **17**(4), 2017. <https://doi.org/10.3390/s17040784>.
36. N. L. Kazanskiy, S. N. Khonina, and M. A. Butt, Plasmonic sensors based on metal-insulator-metal waveguides for refractive index sensing applications: a brief review. *Phys. E Low-Dimensional Syst. Nanostructures* **117**, no. July 2019, 113798 2020. <https://doi.org/10.1016/j.physe.2019.113798>.
37. I. Malkiel, M. Mrejen, A. Nagler, U. Arieli, L. Wolf, H. Suchowski, Plasmonic nanostructure design and characterization via deep learning. *Light Sci. Appl.* **7**(1), 1–8 (2018). <https://doi.org/10.1038/s41377-018-0060-7>
38. I.J. Bigio, S.G. Bown, Spectroscopic sensing of cancer and cancer therapy: current status of translational research. *Cancer Biol. Ther.* **3**, 259–267 (2004). <https://doi.org/10.4161/cbt.3.3.694>
39. B. A. Prabowo, A. Purwidyantri, and K. C. Liu, Surface plasmon resonance optical sensor: a review on light source technology. *Biosensors* **8**(13), (2018). <https://doi.org/10.3390/bios8030080>.
40. E. Fort, Plasmonics. In *Optics in Instruments: Applications in Biology and Medicine* 179–216 2013
41. H. Yu, Y. Peng, Y. Yang, Z.Y. Li, Plasmon-enhanced light–matter interactions and applications. *npj Comput. Mater.* **5**(1), 1–14 (2019). <https://doi.org/10.1038/s41524-019-0184-1>
42. H. Lu, G.X. Wang, X.M. Liu, Manipulation of light in MIM plasmonic waveguide systems. *Chinese Sci. Bull.* **58**(30), 3607–3616 (2013). <https://doi.org/10.1007/s11434-013-5989-6>

43. S. Mehrabani, A.J. Maker, A.M. Armani, Hybrid integrated label-free chemical and biological sensors. *Sensors (Switzerland)* **14**(4), 5890–5928 (2014). <https://doi.org/10.3390/s140405890>
44. A. P. Michael J. Schöning, Label-free biosensing, advanced materials, devices and applications. August 133–178, (2017). <https://doi.org/10.1007/978-3-319-75220-4>.
45. P. Sun, P. Xu, K. Zhu, Z. Zhou, Silicon-based optoelectronics enhanced by hybrid plasmon polaritons: bridging dielectric photonics and nanoplasmonics. *Photonics* **8**(11), (2021). <https://doi.org/10.3390/photonics8110482>.
46. M. Z. Alam, J. S. Aitchison, and M. Mojahedi, Theoretical analysis of hybrid plasmonic waveguide. *IEEE J. Sel. Top. Quantum Electron.* **19**(3), 2013, <https://doi.org/10.1109/JSTQE.2013.2238894>.
47. X. He et al., Ultralow loss graphene-based hybrid plasmonic waveguide with deep-subwavelength confinement. *Opt. Express* **26**(8), 10109 (2018). <https://doi.org/10.1364/oe.26.010109>
48. D. Chelladurai, M. Doderer, U. Koch, Y. Fedoryshyn, C. Haffner, J. Leuthold, Low-loss hybrid plasmonic coupler. *Opt. Express* **27**(8), 11862 (2019). <https://doi.org/10.1364/oe.27.011862>
49. F. Yesilkoy, Optical interrogation techniques for nanophotonic biochemical sensors, *Sensors (Switzerland)* **19**(19), 2019, <https://doi.org/10.3390/s19194287>.
50. L. Jin, M. Li, J. He, S. Member, Analysis of wavelength and intensity interrogation methods in cascaded double-ring sensors. *J. Light. Technol.* **30**(12), 1994–2002 (2012)
51. G. Wang, H. Lu, X. Liu, Y. Gong, L. Wang, Optical bistability in metal-insulator-metal plasmonic waveguide with nanodisk resonator containing Kerr nonlinear medium. *Appl. Opt.* **50**(27), 5287–5290 (2011). <https://doi.org/10.1364/AO.50.005287>
52. P. Sharma and V. Dinesh Kumar, Hybrid insulator metal insulator planar plasmonic waveguide-based components. *IEEE Photonics Technol. Lett.* **29**(16), 1360–1363. 2017. <https://doi.org/10.1109/LPT.2017.2722827>.
53. R.F. Oulton, V.J. Sorger, D.A. Genov, D.F.P. Pile, X. Zhang, A hybrid plasmonic waveguide for subwavelength confinement and long-range propagation. *Nat. Photonics* **2**(8), 496–500 (2008). <https://doi.org/10.1038/nphoton.2008.131>
54. D. Dai, S. He, A silicon-based hybrid plasmonic waveguide with a metal cap for a nano-scale light confinement **17**(19), 496–500 (2009)
55. J.T. Kim, CMOS-compatible hybrid plasmonic waveguide for subwavelength light confinement and on-chip integration **23**(4), 206–208 (2011)
56. E.H.P. Waveguides, Y. Bian, Z. Zheng, Y. Liu, J. Zhu, T. Zhou, Coplanar plasmonic nanolasers based on edge-coupled hybrid plasmonic waveguides. *IEEE PHOTONICS Technol. Lett.* **23**(13), 884–886 (2011)
57. H. Lv, Y. Liu, Z. Yu, C. Ye, and J. Wang, Hybrid plasmonic waveguides for low-threshold nanolaser applications. *CHINESE Opt. Lett.* **12**(11), 112401–1–112401–4 2014. <https://doi.org/10.3788/COL201412.112401>. Since.
58. Z. Wu, R.L. Nelson, J.W. Haus, Q. Zhan, Plasmonic electro-optic modulator design using a resonant metal grating **33**(6), 551–553 (2008)
59. X. Zhang, Fluorescence spectroscopy. 1–19, 2017. <https://doi.org/10.3390/s17122719>.
60. M. F. O. Hameed, S. Member, A. S. Saadeldin, E. M. A. Elkaramany, S. S. A. Obayya, and S. Member, Label-free highly sensitive hybrid plasmonic biosensor for the detection of DNA hybridization. **8724**(c), pp. 1–8 2017. <https://doi.org/10.1109/JLT.2017.2733720>.
61. J.S. Aitchison, M.Z. Alam, X. Sun, M. Mojahedi, Hybrid plasmonic waveguides for on-chip polarization control. *Front. Opt. FIO* **2012**, 2021 (2012). <https://doi.org/10.1364/fio.2012.fth3a.1>
62. L. Luo, C. Xie, X. Wang, Y. Yu, Surface plasmon resonance enhanced highly efficient planar silicon solar cell. *Nano Energy* **9**, 112–120 (2014). <https://doi.org/10.1016/j.nanoen.2014.07.003>
63. J. Gosciniaik and S. I. Bozhevolnyi, Performance of thermo-optic components based on dielectric-loaded surface plasmon polariton waveguides, pp. 3–10, 2013, <https://doi.org/10.1038/srep01803>.
64. M. A. Butt, N. L. Kazanskiy, and S. N. Khonina, Hybrid plasmonic waveguide race-track μ -ring resonator: analysis of dielectric and hybrid mode for refractive index sensing applications. *Laser Phys.* **30**(1), ab5719 2020. <https://doi.org/10.1088/1555-6611/ab5719>.
65. M. Rahmatiyar, M. Afsahi, M. Danaie, Design of a refractive index plasmonic sensor based on a ring resonator coupled to a MIM waveguide containing tapered defects. *Plasmonics* **15**(6), 2169–2176 (2020). <https://doi.org/10.1007/s11468-020-01238-z>
66. T. Wu, Y. Liu, Z. Yu, Y. Peng, C. Shu, H. Ye, The sensing characteristics of plasmonic waveguide with a ring resonator. *Opt. Express* **22**(7), 7669 (2014). <https://doi.org/10.1364/oe.22.007669>
67. N.L. Kazanskiy, S.N. Khonina, M.A. Butt, Plasmonic sensors based on metal-insulator-metal waveguides for refractive index sensing applications : a brief review. *Phys. E Low-dimensional Syst. Nanostructures* (2019). <https://doi.org/10.1016/j.physe.2019.113798>
68. M.A. Butt, S.N. Khonina, N.L. Kazanskiy, Plasmonic refractive index sensor based on metal-insulator-metal waveguides with high sensitivity. *J. Mod. Opt.* **66**(9), 1038–1043 (2019). <https://doi.org/10.1080/09500340.2019.1601272>
69. R. Prakash Dwivedi and E. H. Lee, A compact plasmonic tunable filter using elasto-optic effects, *Opt. Laser Technol.*, vol. 44, no. 7, pp. 2130–2134, 2012, <https://doi.org/10.1016/j.optlastec.2012.03.014>.
70. M.R. Rakhshani, M.A. Mansouri-Birjandi, High sensitivity plasmonic refractive index sensing and its application for human blood group identification. *Sensors Actuators, B Chem.* **249**, 168–176 (2017). <https://doi.org/10.1016/j.snb.2017.04.064>
71. M. A. Butt, S. N. Khonina, and N. L. Kazanskiy, An array of nanodots loaded MIM square ring resonator with enhanced sensitivity at NIR wavelength range. *Optik (Stuttg)* **202**(July 2019), 163655, 2020. <https://doi.org/10.1016/j.ijleo.2019.163655>.
72. M. A. Butt, Plasmonic refractive index sensor based on M-I-M square ring resonator. 2018 Int. Conf. Comput. Electron. Electr. Eng. (ICE Cube), pp. 1–4, 2018.
73. Y. Huang, C. Min, P. Dastmalchi, G. Veronis, Slow-light enhanced subwavelength plasmonic waveguide refractive index sensors. *Opt. Express* **23**(11), 14922 (2015). <https://doi.org/10.1364/oe.23.014922>
74. Y.-F. Chou Chau, Mid-infrared sensing properties of a plasmonic metal-insulator-metal waveguide with a single stub including defects. *J. Phys. D. Appl. Phys.* **53**(11), 115401. 2020.
75. D. I. C. S. Kigin and M. A. L. Ester, Refraction index sensor based on phase resonances in a subwavelength structure with double period. **55**(28), 2016.
76. Y. Chen, Y. Xu, and J. Cao, Fano resonance sensing characteristics of MIM waveguide coupled square convex ring resonator with metallic baffle. *Results Phys.* **149**, 102420, 2019. <https://doi.org/10.1016/j.rinp.2019.102420>.
77. X. Yang, E. Hua, M. Wang, Y. Wang, F. Wen, and S. Yan, Fano resonance in a mim waveguide with two triangle stubs coupled with a split-ring nanocavity for sensing application. *Sensors (Switzerland)* **19**(22), 2019. <https://doi.org/10.3390/s19224972>.
78. R. Zafar, M. Salim, Enhanced figure of merit in Fano resonance-based plasmonic refractive index sensor. *IEEE Sens. J.* **15**(11), 6313–6317 (2015). <https://doi.org/10.1109/JSEN.2015.2455534>
79. P. Debackere, S. Scheerlinck, P. Bientman, R. Baets, Surface plasmon interferometer in silicon-on-insulator: novel concept for an integrated biosensor. *Opt. Express* **15**(21), 13651 (2007). <https://doi.org/10.1364/oe.15.013651>

80. J. Leuermann et al., Optimizing the limit of detection of waveguide-based interferometric biosensor devices. *Sensors (Switzerland)* **19**(17), 1–13 (2019). <https://doi.org/10.3390/s19173671>
81. J. Costa, A. Fantoni, P. Lourenço, and M. Vieira, Simulation of a parallel waveguide array structure suitable for interrogation scheme in a plasmonic biosensor. no. March 2020, p. 83, 2020. <https://doi.org/10.1117/12.2546178>.
82. B.H. Lee et al., Interferometric fiber optic sensors. *Sensors* **12**(3), 2467–2486 (2012). <https://doi.org/10.3390/s120302467>
83. J. Homola, Surface plasmon resonance sensors for detection of chemical and biological species. *Chem. Rev.* **108**(2), 462–493 (2008). <https://doi.org/10.1021/cr068107d>
84. S. Luo, B. Li, D. Xiong, D. Zuo, X. Wang, A high performance plasmonic sensor based on metal-insulator-metal waveguide coupled with a double-cavity structure. *Plasmonics* **12**(2), 223–227 (2017). <https://doi.org/10.1007/s11468-016-0253-y>
85. Z. Zhang et al., Plasmonic refractive index sensor with high figure of merit based on concentric-rings resonator. *Sensors (Switzerland)* **18**(1), 2018. <https://doi.org/10.3390/s18010116>.
86. R. Adhikari, D. Chauhan, G.T. Mola, R.P. Dwivedi, A review of the current state-of-the-art in Fano resonance-based plasmonic metal-insulator-metal waveguides for sensing applications. *Opto-Electronics Rev.* **29**(4), 148–166 (2021). <https://doi.org/10.24425/opelre.2021.139601>
87. H. Ben, A. Hocini, M.N. Temmar, D. Khedrouche, Design of mid infrared high sensitive metal-insulator-metal plasmonic sensor. *Chinese J. Phys.* **61**(August), 86–97 (2019). <https://doi.org/10.1016/j.cjph.2019.07.006>
88. G.A. López-muñoz et al., A label-free nanostructured plasmonic biosensor based on Blu-ray discs with integrated micro fluidics for sensitive biodetection. *Biosens. Bioelectron.* **96**(May), 260–267 (2017). <https://doi.org/10.1016/j.bios.2017.05.020>
89. M.R. Rakhshani, M.A. Mansouri-Birjandi, Engineering hexagonal array of nanoholes for high sensitivity biosensor and application for human blood group detection. *IEEE Trans. Nanotechnol.* **17**(3), 475–481 (2018). <https://doi.org/10.1109/TNANO.2018.2811800>
90. M.R. Rakhshani, M.A. Mansouri-Birjandi, High-sensitivity plasmonic sensor based on metal-insulator-metal waveguide and hexagonal-ring cavity. *IEEE Sens. J.* **16**(9), 3041–3046 (2016). <https://doi.org/10.1109/JSEN.2016.2522560>
91. M.A. Butt, S.N. Khonina, N.L. Kazanskiy, Metal-insulator-metal nano square ring resonator for gas sensing applications. *Waves in Random and Complex Media* **31**(1), 146–156 (2021). <https://doi.org/10.1080/17455030.2019.1568609>
92. M. A. Butt, S. N. Khonina, and N. L. Kazanskiy, Plasmonic refractive index sensor based on M-I-M square ring resonator. 2018 Int. Conf. Comput. Electron. Electr. Eng. ICE Cube 2018, January, pp. 1–4, 2019. <https://doi.org/10.1109/ICECUBE.2018.8610998>.
93. R. Al Mahmud, M. O. Faruque, and R. H. Sagor, A highly sensitive plasmonic refractive index sensor based on triangular resonator. *Opt. Commun.* **483**, 126634, 2021. <https://doi.org/10.1016/j.optcom.2020.126634>.
94. Z. Guo, K. Wen, Q. Hu, W. Lai, J. Lin, and Y. Fang, Plasmonic multichannel refractive index sensor based on subwavelength tangent-ring metal-insulator-metal waveguide. *Sensors (Switzerland)* **18**(5), 2018. <https://doi.org/10.3390/s18051348>.
95. G. Cao, H. Li, Y. Deng, S. Zhan, Z. He, B. Li, Plasmon-induced transparency in a single multimode stub resonator **22**(21), 9198–9205 (2014). <https://doi.org/10.1364/OE.22.025215>
96. R.D. Kekatpure, E.S. Barnard, W. Cai, M.L. Brongersma, Phase-coupled plasmon-induced transparency **243902**(June), 1–4 (2010). <https://doi.org/10.1103/PhysRevLett.104.243902>
97. A. Lezama, S. Barreiro, A.M. Akulshin, Electromagnetically induced absorption **59**(6), 4732–4735 (1999)
98. J. Tian, J. Li, Investigation on plasmon induced transparency and its application in an MIM type compound plasmonic waveguide. *Prog. Electromagn. Res. C* **98**(January), 199–212 (2020). <https://doi.org/10.2528/pierc19102001>
99. Y. Bin Feng, H. Guohua, Z. Ruohu, C. Yiping, Design of a compact and high sensitive refractive index sensor base on metal-insulator-metal plasmonic Bragg grating. *Opt. Express* **22**(23), 28662 (2014). <https://doi.org/10.1364/oe.22.028662>
100. Y. F. C. Chau, C. T. C. Chao, H. J. Huang, N. T. R. N. Kumara, C. M. Lim, H. P. Chiang, Ultra-high refractive index sensing structure based on a metal-insulator-metal waveguide-coupled T-shape cavity with metal nanorod defects. *Nanomaterials* **(9)**10, (2019). <https://doi.org/10.3390/nano9101433>.
101. J. Yin, J. Tian, R. Yang, Investigation of the transmission properties of a plasmonic MIM waveguide coupled with two ring resonators. *Mater. Res. Express* **6**(3), 2021 (2019). <https://doi.org/10.1088/2053-1591/aaf483>
102. R. Zafar, S. Nawaz, G. Singh, A. D’Alessandro, M. Salim, Plasmonics-based refractive index sensor for detection of hemoglobin concentration. *IEEE Sens. J.* **18**(11), 4372–4377 (2018). <https://doi.org/10.1109/JSEN.2018.2826040>
103. M.R. Rakhshani, M.A. Mansouri-Birjandi, A high-sensitivity sensor based on three-dimensional metal-insulator-metal race-track resonator and application for hemoglobin detection. *Photonics Nanostructures - Fundam. Appl.* **32**, 28–34 (2018). <https://doi.org/10.1016/j.photonics.2018.08.002>
104. X. Li et al., Tunable plasmonically induced reflection in HRR-coupled MIM waveguide structure. *Optik (Stuttg.)* **199**(September), 163353 (2019). <https://doi.org/10.1016/j.jileo.2019.163353>.
105. M.A. Butt, N.L. Kazanskiy, S.N. Khonina, Highly sensitive refractive index sensor based on plasmonic bow tie configuration. *Photonic Sensors* **10**(3), 223–232 (2020). <https://doi.org/10.1007/s13320-020-0588-z>
106. N. L. Kazanskiy, M. A. Butt, S. N. Khonina, Nanodots decorated MIM semi-ring resonator cavity for biochemical sensing applications. *Photonics Nanostructures - Fundam. Appl.* **42**(August), 100836 (2020). <https://doi.org/10.1016/j.photonics.2020.100836>.
107. S. Zhan et al., Tunable nanoplasmonic sensor based on the asymmetric degree of Fano resonance in MDM waveguide. *Sci. Rep.* **6**(March), 1–8 (2016). <https://doi.org/10.1038/srep22428>
108. L. Chen et al., Numerical analysis of a near-infrared plasmonic refractive index sensor with high figure of merit based on a fillet cavity. *Opt. Express* **24**(9), 9975 (2016). <https://doi.org/10.1364/oe.24.009975>
109. S. Bin Yan, L. Luo, C. Y. Xue, Z. D. Zhang, A refractive index sensor based on a metal-insulator-metal waveguide-coupled ring resonator. *Sensors (Switzerland)* **15**(11), 29183–29191 (2015). <https://doi.org/10.3390/s151129183>.
110. Y.S. Zhou, B.Y. Gu, H.Y. Wang, Band-gap structures of surface-plasmon polaritons in a subwavelength metal slit filled with periodic dielectrics. *Phys. Rev. A* **81**(1), 015801 (2010). <https://doi.org/10.1103/PhysRevA.81.015801>
111. Z.M. Meng, F. Qin, Realizing prominent Fano resonances in metal-insulator-metal plasmonic Bragg gratings side-coupled with plasmonic nanocavities. *Plasmonics* **13**(6), 2329–2336 (2018). <https://doi.org/10.1007/s11468-018-0756-9>
112. J. Zhu, G. Wang, Sense high refractive index sensitivity with bragg grating and MIM nanocavity. *Results Phys.* **10**, 102763 (2019). <https://doi.org/10.1016/j.rinp.2019.102763>.
113. Y. Bin Feng, H. Guohua, Z. Ruohu, C. Yiping, Design of a compact and high sensitive refractive index sensor base on metal-insulator-metal plasmonic Bragg grating **22**(23), 1217–1222 (2014). <https://doi.org/10.1364/OE.22.028662>
114. H. Guner et al., A smartphone based surface plasmon resonance imaging (SPRi) platform for on-site biodetection. *Sensors Actuators B. Chem.* **239**, 571–577 (2017). <https://doi.org/10.1016/j.snb.2016.08.061>

115. K. He, Y. Liu, Y. Fu, Transmit-array, metasurface-based tunable polarizer and high-performance biosensor in the visible regime. *Nanomaterials* **9**(4), 603 (2019). <https://doi.org/10.3390/nano9040603>
116. M. Shen, M. Wang, J. Zhou, L. Du, C. Deng, Nanostructured plasmonic interferometers for compact sensing. *Plasmonics* (2016). <https://doi.org/10.1007/s11468-016-0315-1>.
117. X. Gu, R. Bai, X.R. Jin, Y.Q. Zhang, S. Zhang, Y. Lee, Ultranarrow-band perfect absorber based on high-order plasmonic resonance in metamaterial. *J. Nonlinear Opt. Phys. Mater.* **25**(1), 1650011 (2016). <https://doi.org/10.1142/S0218863516500119>
118. A.K. Sharma, A.K. Pandey, Metal oxide grating based plasmonic refractive index sensor with Si layer in optical communication band. *IEEE Sens. J.* **20**(3), 1275–1282 (2020). <https://doi.org/10.1109/JSEN.2019.2947627>
119. M.J. Al-mahmod, R. Hyder, M.Z. Islam, Numerical studies on a plasmonic temperature nanosensor based on a metal-insulator-metal ring resonator structure for optical integrated circuit applications. *Photonics Nanostructures - Fundam. Appl.* **25**, 52–57 (2017). <https://doi.org/10.1016/j.photonics.2017.05.001>
120. N.L. Kazanskiy, S.N. Khonina, M.A. Butt, A. Kaźmierczak, R. Piramidowicz, A numerical investigation of a plasmonic sensor based on a metal-insulator-metal waveguide for simultaneous detection of biological analytes and ambient temperature. *Nanomaterials* **11**(10), 2551 (2021). <https://doi.org/10.3390/nano11102551>
121. P. Steglich et al., Hybrid-waveguide ring resonator for biochemical sensing. *IEEE Sens. J.* **17**(15), 4781–4790 (2017). <https://doi.org/10.1109/JSEN.2017.2710318>
122. M.A. Butt, S.N. Khonina, N.L. Kazanskiy, Sensitivity enhancement of silicon strip waveguide ring resonator by incorporating a thin metal film. *IEEE Sens. J.* **20**(3), 1355–1362 (2020). <https://doi.org/10.1109/JSEN.2019.2944391>
123. X. Sun, D. Dai, L. Thylén, L. Wosinski, Double-slot hybrid plasmonic ring resonator used for optical sensors and modulators. *Photonics* **2**(4), 1116–1130 (2015). <https://doi.org/10.3390/photronics2041116>
124. M.A. Butt, S.N. Khonina, N.L. Kazanskiy, Hybrid plasmonic waveguide-assisted metal-insulator-metal ring resonator for refractive index sensing. *J. Mod. Opt.* **65**(9), 1135–1140 (2018). <https://doi.org/10.1080/09500340.2018.1427290>
125. M.A. Butt, N.L. Kazanskiy, S.N. Khonina, Modal characteristics of refractive index engineered hybrid plasmonic waveguide. *IEEE Sens. J.* **20**(17), 9779–9786 (2020). <https://doi.org/10.1109/JSEN.2020.2991215>
126. N.L. Kazanskiy, S.N. Khonina, M.A. Butt, Subwavelength grating double slot waveguide racetrack ring resonator for refractive index sensing application. *Sensors (Switzerland)* **20**(12), 1–13 (2020). <https://doi.org/10.3390/s20123416>
127. M.A. Butt, S.N. Khonina, N.L. Kazanskiy, Highly sensitive refractive index sensor based on hybrid plasmonic waveguide microring resonator. *Waves in Random and Complex Media* **30**(2), 292–299 (2020). <https://doi.org/10.1080/17455030.2018.1506191>
128. K. M. Weerakoon-ratnayake, S. Vaidyanathan, C. A. Amarasekara, C. K. Johnson, S. A. Soper, Single molecule analysis in nanofluidic devices, in *Elsevier*, Elsevier Inc. 335–377 (2019).
129. A. Rahim et al., Open-access silicon photonics platforms in Europe. *IEEE J. Sel. Top. Quantum Electron.* **25**(5), 1–18 (2019). <https://doi.org/10.1109/JSTQE.2019.2915949>

Publisher's Note Springer Nature remains neutral with regard to jurisdictional claims in published maps and institutional affiliations.